Weierstraß-Institut
für Angewandte Analysis und Stochastik
Leibniz-Institut im Forschungsverbund Berlin e. V.

Preprint ISSN 2198-5855

Traveling wave modeling of nonlinear dynamics in multisection semiconductor lasers

Mindaugas Radziunas[1]

submitted: May 10, 2016

[1] Weierstrass Institute
Mohrenstr. 39
10117 Berlin
Germany
E-Mail: Mindaugas.Radziunas@wias-berlin.de

No. 2261
Berlin 2016

2010 *Mathematics Subject Classification.* 78A60 35Q60 78M34 37N20 78-04 35-04.

2008 *Physics and Astronomy Classification Scheme.* 42.55.Px 42.60.-v 02.30.Jr 02.30.Oz 02.60.Cb.

Key words and phrases. traveling wave model, semiconductor laser, narrow waveguide, edge emitting laser, multisection laser, ring laser, simulations, analysis.

Edited by
Weierstraß-Institut für Angewandte Analysis und Stochastik (WIAS)
Leibniz-Institut im Forschungsverbund Berlin e. V.
Mohrenstraße 39
10117 Berlin
Germany

Fax: +49 30 20372-303
E-Mail: preprint@wias-berlin.de
World Wide Web: http://www.wias-berlin.de/

Abstract

A hierarchy of 1 (time) + 1 (space) dimensional first-order partial differential equation (traveling wave) models is used for a description of dynamics in individual semiconductor lasers, various multisection semiconductor lasers, and coupled laser systems. Consequent modifications of the basic traveling wave model allow for taking into account different physical effects such as the gain dispersion, the thermal detuning, the spatial hole burning of carriers, the nonlinear gain saturation, or various carrier exchange processes in quantum dot lasers. For illustration, the model was applied for simulations of dynamics in complex ring laser with four branches of filtered feedback. Finally, several advanced techniques for model analysis such as calculation of instantaneous optical modes, finding of steady states, and numerical continuation and bifurcation analysis of the model equations were discussed and illustrated by example simulations.

1 Introduction

Narrow waveguide edge-emitting semiconductor lasers are attractive devices for different applications. Among others, these are high-speed all-optical signal processing, optical data storage, thermal and xerographic printing, scanning, directional lighting, secure communications, random number generation, frequency conversion, or various interferometric, spectroscopic, instrumentation and other quantum-optical experiments.

A typical solitary narrow-waveguide (single transversal mode) semiconductor laser exhibits a single-wavelength emission required in different applications. In many cases, however, small fluctuations of the operation conditions impose a significant phase noise which, in turn, causes an unwanted broadening of the emission linewidth. Moreover, the stable performance of the laser can be easily violated by optically reinjected light, and there is a huge number of studies devoted to the analysis of the nonlinear dynamics in lasers with a delayed optical feedback.

A properly designed optical feedback, however, can also play a constructive role when seeking to improve an operation of the solitary laser, or create a new dynamical regime. For example, an external cavity with a diffractive grating can be used for emission linewidth reduction or tuning of the lasing wavelength [1]. Or, on the contrary, specially designed external cavities allow realizing a chaotic emission usable for cryptography [2] or random number generation [3].

Multisection semiconductor lasers (MSLs) in linear or ring configurations and coupled laser devices provide even more possibilities to tailor laser dynamics for certain applications. For example, a variety of important functionalities of the optical data communications [4] such as pulse generation, clock recovery, and fast switching can be realized by specially designed and

differently interconnected MSLs. Several examples of theoretically investigated and experimentally verified dynamic performance of MSLs considered in our previous papers are excitability [5], high-frequency mode-beating pulsations [6], and modulation band enhancement [7] in distributed feedback (DFB) lasers with an integrated passive phase tuning section (passive feedback lasers); passive [8] or hybrid [9] harmonic and sub-harmonic mode-locking in lasers with saturable absorber, and pulse broadening in quantum-dot (QD) mode-locked lasers [10]; tunable high-frequency pulsations in the detuned grating DFB lasers with an integrated phase tuning section (phase controlled mode beating lasers) [11, 12]; stationary, pulsating and irregular regimes and their bifurcations in DFB lasers with integrated phase tuning and amplifying sections (active feedback laser) [6, 13]; Joule heating induced transitions between steady states in distributed Bragg reflector (DBR) lasers [14] or external cavity diode lasers (ECDLs) [15].

All these examples confirm the practical importance of modeling, simulations and analysis of MSLs for designing new devices with a particular dynamical behavior. The most precise models usually are given by 2+1 or 3+1 dimensional systems of partial differential equations (PDEs) [16, 17]. The numerical simulations in this case, however, are time-consuming, whereas application of analytic methods for the analysis of the nonlinear dynamics is very limited. Unfortunately, numerical simulations of such models are time-consuming, whereas an application of analytic methods for the model analysis is very limited. For this reason, we prefer to use simpler approaches which, may be, fail to reproduce a quantitative-, but still allow to get a qualitative agreement between theory and experiments.

For some MSLs, already simple ordinary differential equation (ODE) or delay differential equation (DDE) systems [rate equations] admit a reasonable description of the laser dynamics. An advantage of these models is their simplicity allowing fast numerical simulations and application of advanced analytic methods, such as asymptotic analysis, stability analysis, or numerical continuation and bifurcation analysis. These models, however, usually are based on mean-field approximations, i.e., neglect inhomogeneity of laser parameters and dynamical variables along the laser cavity, take into account only a few fundamental characteristics of the considered lasers, or are suited to describe particular MSL configurations [18, 19, 20].

The 1+1-dimensional traveling wave (TW) model considered in this work is a compromise between simplicity and precision. It is a first-order PDE system having a single spatial dimension corresponding to the longitudinal (z-) direction along the laser cavity and describing dynamics of the slowly varying optical field amplitudes, polarization functions, and carrier density [21, 22, 23]. Comparing to ODE and DDE models mentioned above, the TW model is computationally more demanding but still enables an advanced analysis, which is hardly possible in the case of the multidimensional PDE models.

By taking into account or neglecting different physical effects, one can derive a whole hierarchy of TW models of different complexity. The standard part of all such models is a pair of TW equations governing the evolution of the complex forward- and back- propagating field amplitudes, $E^+(z,t)$ and $E^-(z,t)$. These equations originate from the decomposition of the dominant fundamental transverse electric (TE) component of the electromagnetic wave,

$$E(\mathbf{r},t) = \Phi(x,y)\left[E^+(z,t)e^{-ik_0 z} + E^-(z,t)e^{ik_0 z}\right]e^{i\omega_0 t}.$$

Here, ω_0 is the central reference frequency and k_0 is the corresponding wave vector. Whereas

the transversal waveguide mode profile, $\Phi(x, y)$, is an eigensolution of the waveguide equation, the related complex eigenvalue of the same problem defines the propagation factor β [24], which determines the evolution of the field amplitudes $E^{\pm}$. In general, the propagation factor depends on the complex interaction of carriers and photons. In our modeling approach, we apply a phenomenological dependence of this factor on the real carrier density function N, which can represent dynamics of the spatially distributed carrier density, $N(z, t)$, or the section-wise averaged density, $N(t)$. The evolution of N itself is governed by a single or several rate equations.

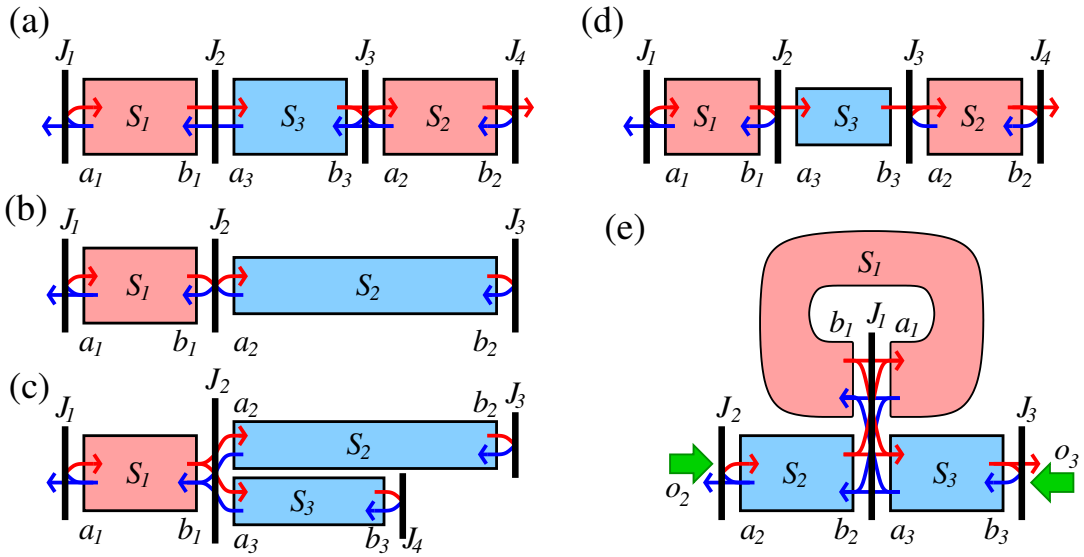

Figure 1: Schematic representation of five semiconductor laser devices which can be considered by our modeling approach. (a): Three-section laser. (b): Laser with a trivial external cavity. (c): Laser with a dual external cavity. (d): Master-slave laser system. (e): Optically injected ring laser with an outcoupling waveguide. Pink and light blue frames represent active and passive *sections* (S_*) of the MSL. Thick black segments and thick green arrows indicate *junctions* (interfaces of these sections, J_*) and *optical injections* (o_*), respectively. Thin arrows show optical field transmissions and reflections at the interfaces of the laser sections.

One can use the TW modeling approach for consideration of various differently interconnected linear and curved, active and passive semiconductor waveguiding parts, taking into account optical injections, field reflections and transmissions at the interfaces of different laser parts, as well as delayed feedback of the optical fields from the external cavities. For simulation and analysis of the MSLs, we apply our software LDSL-tool [25], which is suited to investigate the (L)ongitudinal (D)ynamics of multisection (S)emiconductor (L)asers. This software allows considering a large variety of MSL devices or coupled laser systems which can be represented by a set of mutually interconnected *sections* and *junctions*, see schematic representations of several laser devices in Fig. 1. Besides of numerical integration, LDSL-tool can find longitudinal optical modes and analyze their dynamics [26, 23]. In some cases, it locates stable and unstable stationary states of the system [27, 15], constructs the reduced ODE models based on a finite number of the optical modes [28], and, together with the software package AUTO [29], performs numerical continuation and bifurcation analysis of these reduced models [7].

In following, we shall introduce a basic TW model for the solitary laser, and present several model extensions allowing to take into account initially neglected physical effects. Next, we shall discuss a possibility to join several laser sections into a single multisection laser or a coupled laser device. For an illustration of the available device complexity, we shall present simulations of a ring laser with four branches of filtered feedback. At the last part of this work, we shall briefly introduce the concept of the instantaneous optical modes, discuss the mode analysis, the location and semi-analytic continuation of the stationary states, the model reduction, and the numerical bifurcation analysis.

2 Basic TW model in the solitary laser

Below in this section, we formulate the simplest TW model suitable for simulations of a solitary semiconductor laser. Let us consider an edge-emitting narrow-waveguide semiconductor laser [see Fig. 2(a)]. According to our notations, the "interior" part of this laser is referred as *section* S_1. The longitudinal coordinates of the section edges and the length of this section are $z = a_1$, $z = b_1$, and $|S_1| = b_1 - a_1$, respectively. The front and the rear laser facets (*junctions* J_1 and J_2), in this case, correspond to the left and the right edges a_1 and b_1 of S_1.

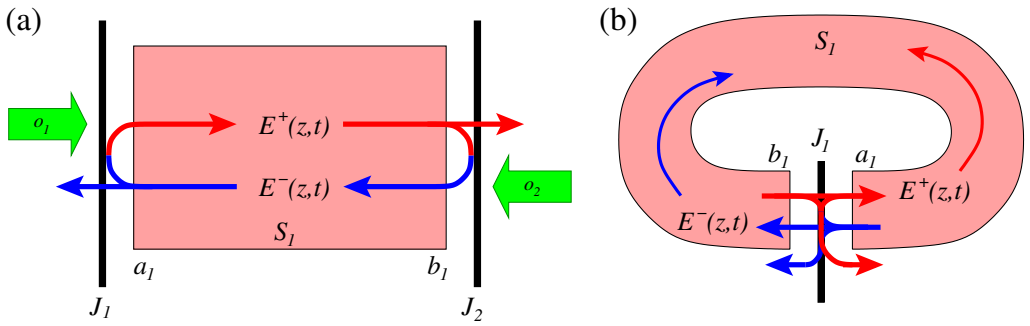

Figure 2: Schematic representation of the single section lasers in linear (a) and ring (b) configurations. Thin arrows indicate directions of the counter-propagating fields and their reflections/transmissions at the laser facets (J_1 and J_2, panel (a)) or point outcoupling interface (J_1, panel (b)). Thick green arrows represent optically injected fields.

The backbone of the TW model of this laser is the linear system of partial differential (traveling wave) equations describing an evolution of the slowly varying complex amplitudes $E^+(z,t)$ and $E^-(z,t)$ of the counter-propagating optical fields:

$$\begin{cases} \frac{n_g}{c_0}\partial_t E^+ + \partial_z E^+ = -i\beta E^+ - i\kappa E^- + F^+_{sp} \\ \frac{n_g}{c_0}\partial_t E^- - \partial_z E^- = -i\beta E^- - i\kappa E^+ + F^-_{sp} \end{cases}, \quad z \in S_1. \tag{1}$$

Here, c_0 is the speed of light in vacuum, $F^{\pm}_{sp}$ are the Langevin noise source contributions to the optical fields, and n_g is the group velocity index. The real and the imaginary parts of the complex coefficient κ represent the distributed index and gain/loss coupling of the counter-propagating fields, respectively. κ is non-vanishing in the laser sections containing Bragg grating and is set

to zero in the straight sections without the grating. Without an additional scaling of the field functions $E^{\pm}$, $|E(z,t)|^2 = (E,E) = |E^+|^2 + |E^-|^2$ represents the photon density and is proportional to the local field power,

$$\mathcal{P}(z,t) = \frac{\sigma c_0}{n_g}\frac{hc_0}{\lambda_0}|E(z,t)|^2.$$

Here, σ is the cross-section area of the active zone, λ_0 is the central wavelength, and h is the Planck constant.

Active sections. The propagation factor β in the TW equations above can be defined as

$$\beta = \delta_0 + \tilde{n}(N) + \frac{i(g(N)-\alpha)}{2}, \tag{2}$$

where the peak gain and refractive index change functions $g(N)$ and $\tilde{n}(N)$ are given by the simple linear relations,

$$g(N) = \Gamma g'\left(N - N_{\text{tr}}\right), \qquad \tilde{n}(N) = \frac{\alpha_H g(N)}{2}. \tag{3}$$

Here, N is the carrier density. Parameters δ_0, α, Γ, g', and α_H are the internal field loss, the initial fixed detuning from the central frequency, the confinement factor, the differential gain, and the linewidth enhancement (Henry) factor evaluated at the transparency carrier density N_{tr}.

To define the evolution of the spatially averaged carrier density $N(t)$, we use a single rate equation

$$\frac{d}{dt}N = \frac{I}{q\sigma|S_1|} - \mathcal{R}(N) - \mathcal{S}(N,E^{\pm}). \tag{4}$$

Here, q is the electron charge, I is the injected current into the active zone of the section, whereas $\mathcal{R}$ and $\mathcal{S}$ are spontaneous and stimulated recombination functions, respectively. We use a cubic spontaneous recombination function,

$$\mathcal{R}(N) = AN + BN^2 + CN^3, \tag{5}$$

which can be simplified by assuming vanishing recombination parameters B and C and defining $A = \tau_N^{-1}$, where τ_N denotes the carrier lifetime. Function $\mathcal{S}$ in the carrier rate equation (4) represents the spatially averaged stimulated recombination:

$$\mathcal{S}(N,E^{\pm}) = \frac{c_0}{n_g}g(N)\|E\|_1^2. \tag{6}$$

Here, $\|E\|_1^2$ is the spatial average of the local photon density along the section S_1,

$$\|E\|_1^2 = \langle (E,E)\rangle_1, \qquad \langle\eta\rangle_1 = \frac{1}{|S_1|}\int_{S_1}\eta(z)dz, \qquad (\zeta,\xi) = \zeta^{+*}\xi^{+} + \zeta^{-*}\xi^{-},$$

and * denotes the complex conjugate.

To complete the system, we still need to define the incident forward- and backward- propagating fields at the section edges $z = a_1$ and $z = b_1$, respectively. For the solitary laser, these incident fields can be defined by the following reflection/transmission conditions:

$$E^+(a_1,t) = -r_1^* E^-(a_1,t) + o_1(t), \;\; E^-(b_1,t) = r_2 E^+(b_1,t) + o_2(t). \tag{7}$$

Here, r_1 and r_2 are the complex field amplitude reflectivity coefficients at the laser facets (junctions J_1 and J_2), whereas complex functions $o_{1,2}(t)$ represent optical injections at these junctions.

One can also use the model equations (1), (2), (3), (4), (5), (6) for simulations of narrow-waveguide semiconductor ring lasers with the field in- and out- coupling concentrated in the single point of this laser. Fig. 2(b) shows a schematic representation of such single-section ring laser device. According to this scheme, we assume that both, "left" and "right" edges a_1 and b_1 of the section S_1, are connected at the single junction J_1. The boundary conditions (7), in this case, should be replaced by the following field transmission-reflection conditions at J_1:

$$E^+(a_1,t) = t_1 E^+(b_1,t) - r_1^* E^-(a_1,t), \;\; E^-(b_1,t) = t_1 E^-(a_1,t) + r_1 E^+(b_1,t). \quad (8)$$

Here, t_1 is the real field amplitude transmission factor back into the ring section S_1 at the out-coupling point J_1, whereas the complex factor r_1 represents the localized field backscattering at J_1.

To perform simulations of the basic TW model equations, (1), (2), (3), (4), (5), (6), (7) or (8), one still needs to choose some initial conditions $E^{\pm}(z,0)$ and $N(0)$. For the first run of simulations, one can use any small distribution of the optical fields $E^{\pm}(z,0)$ and a small positive value of $N(0)$. After some transient, the computed trajectory will be attracted by one of the few regular or irregular attractors of the considered dissipative system. To keep tracing the same attractor during the following parameter continuation calculations, one should better use previously obtained carrier density and field distributions.

Passive sections. It is noteworthy that one can also use the TW equations (1) for a description of the field propagation in the passive sections, such as gratings, free space between the laser and the external mirror, etc.. Here, carriers are absent, do not couple to the emission wavelength (the material gain band of these sections does not support the lasing frequencies), or are just kept at transparency level by an appropriately adjusted bias current. In all such cases, $g(N) = \tilde{n}(N) = 0$, the carrier rate equations (4) are decoupled from the field equations (1) and, therefore, are irrelevant.

In the case of the passive section S_k containing no grating ($\kappa = 0$), simple analytic relations of the field function values on the both sides of S_k,

$$\begin{aligned} &E^+(b_k,t) = \eta e^{i\varphi/2} E^+(a_k, t-\tau_k), \quad E^-(a_k,t) = \eta e^{i\varphi/2} E^-(b_k, t-\tau_k), \quad \text{where} \\ &\tau_k = \tfrac{|S_k| n_g}{c_0}, \quad \eta = e^{-\alpha |S_k|/2}, \quad \varphi = -2\delta_0 |S_k|, \end{aligned} \quad (9)$$

can replace the field equations (1).

In the case of the passive grating ($\kappa \neq 0$), the analytic solution of the field equations (1) in the frequency domain is given by the 2×2 dimensional transfer matrix M [26, 28, 23],

$$\widehat{E}(z,\omega) = M(\beta, \kappa, \omega; z, a_k) \widehat{E}(a_k, \omega). \quad (10)$$

Here, $\beta = \delta_0 - i\alpha/2$, ω is the relative frequency, $\widehat{E}(z,\omega) = \left(\widehat{E}^+, \widehat{E}^-\right)^T$, ^{T} denotes the transpose vector, whereas $\widehat{E}^{\pm}$ are the frequency domain representations of the fields $E^{\pm}(z,t)$.

Within any interval $[z', z]$ where parameters β and κ are constant, the matrix M is defined by

$$M(\beta,\kappa,\omega;z,z') = \begin{pmatrix} \cos\eta(z-z') - \frac{i\mathcal{B}}{\eta}\sin\eta(z-z') & -\frac{i\kappa}{\eta}\sin\eta(z-z') \\ \frac{i\kappa}{\eta}\sin\eta(z-z') & \cos\eta(z-z') + \frac{i\mathcal{B}}{\eta}\sin\eta(z-z') \end{pmatrix},$$
$$\mathcal{B}(\omega) = \beta + \tfrac{\omega n_g}{c_0}, \qquad \eta = \sqrt{\mathcal{B}^2 - \kappa^2}. \tag{11}$$

Once the parameters β or κ are peace-wise constants, i.e., constant within each small subinterval $[z_s, z_{s-1}]$, $z' = z_0 < z_1 < \cdots < z_n = z$, the transfer matrix M is the superposition of corresponding transfer matrices over these small subintervals:

$$M(\beta,\kappa,\omega;z,z') = M_n \times \cdots \times M_1, \quad M_s = M(\beta(z_{s-1/2}),\kappa(z_{s-1/2}),\omega;z_s,z_{s-1}). \tag{12}$$

3 Model of material gain dispersion

The relations (3) introduced in Section 2 are simple linear approximations of the gain and refractive index functions G and $\tilde{N}$. In general, these functions depend not only on the carrier density N, but also on the optical frequency ω, field intensities $|E^+|^2$ and $|E^-|^2$, and some other physical effects, such as temperature, not considered in our modeling approach. In this section, we introduce the model of the gain dispersion of the semiconductor material, which restricts the gain band in the frequency domain and is the primary optical frequency selection mechanism in Fabry-Perot (FP) lasers.

Before switching to the modeling of the gain dispersion, let us find out the expression of the laser response $F_l(b_1,\omega)$ to the incident plane wave $e^{i\omega t}$ applied to the right edge of the device [see Fig. 3(a)]. For this reason, we freeze the propagation factor β and substitute the ansatz $E^{\pm}(z,t) = \widehat{E}^{\pm}(z,\omega)e^{i\omega t}$ into the field equations (1). The solution of the resulting system of ODEs within S_1 can be represented by Eq. (10), where the transfer matrix M is defined in (11). The ratio of the outgoing and incident waves at $z = b_1$ together with the (non-injective) boundary condition (7) at $z = a_1$ define the function $F_l(b_1,\omega)$ which shows the laser response in dependence on the optical frequency of the injected field[1]. In two simple cases of FP lasers and DFB lasers with vanishing facet reflectivity, the response function is given by

$$F_l(b_1,\omega) = \frac{\widehat{E}^+(b_1,\omega)}{\widehat{E}^-(b_1,\omega)} = \begin{cases} -r_1^* e^{-2i\beta|S_1|}e^{-i2\omega n_g|S_1|/c_0}, & \kappa = 0,\ r_1 \neq 0 \ \text{(FP laser)} \\ \frac{\kappa}{i\eta(\omega)\cot[|S_1|\eta(\omega)]-\mathcal{B}(\omega)}, & \kappa \neq 0,\ r_1 = 0 \ \text{(DFB laser)} \end{cases}. \tag{13}$$

Figs. 3(b) and (c) show the intensities of these response functions in FP and DFB lasers calculated for different values of carrier densities N. Note also, that the abscissa axis in these figures represents relative wavelengths λ related to the relative frequencies ω by formula $\lambda \approx -\frac{\lambda_0^2}{2\pi c_0}\omega$.

The flat laser response curves in Fig. 3(b) indicate an absence of frequency selection mechanisms for FP lasers in our fundamental TW model. Thus, this simple model is not suitable for

[1] In the same way, one can also define the response function $F_r(a_1,\omega)$ at the left side of the laser

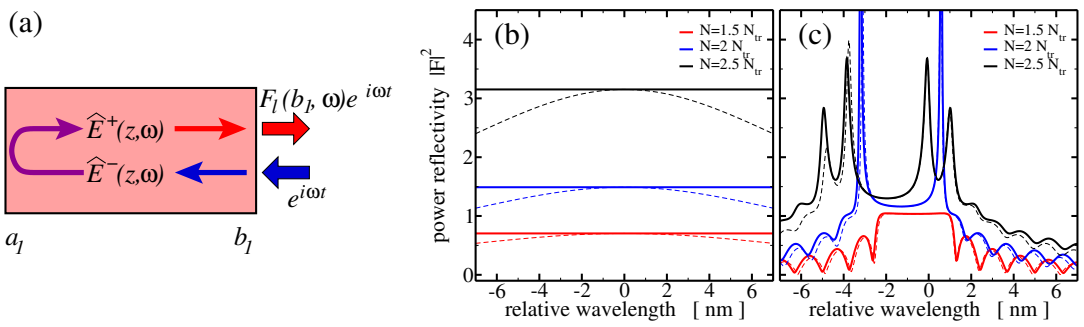

Figure 3: Laser response to the incident plane wave $e^{i\omega t}$. (a): Schematic representation. Thin and thick arrows show field propagation directions and incident/emitted optical fields. (b): Response intensity of the solitary FP laser. Parameters $\lambda_0 = 1.57\,\mu$m, $|S_1| = 0.25$ mm, $n_g = 3.6$, $\delta_0 = 0$, $\alpha = 20\,\text{cm}^{-1}$, $\alpha_H = -4$, $\Gamma = 0.15$, $g' = 4\cdot 10^{-16}\,\text{cm}^2$, $N_{\text{tr}} = 10^{18}\,\text{cm}^{-3}$, $r_1 = r_2 = \sqrt{0.3}$, $\kappa = 0$. (c): Response intensity of the solitary DFB laser. Parameters are the same as in (b), only $\kappa = 130\,\text{cm}^{-1}$ and $r_1 = r_2 = 0$. Dashed and solid curves in panels (b) and (c) represent models with ($\bar{g} = 100\,\text{cm}^{-1}$, $\bar{\lambda} = 0$, $\bar{\gamma}_\lambda = 40$ nm) and without ($\bar{g} = 0$) gain dispersion.

simulations of FP lasers. In contrast, the wavelength selection in DFB lasers is mainly determined by the Bragg grating, and numerical integration of the TW model can provide reliable information. One should note, however, that the index-coupled DFB laser (characterized by a real coupling factor κ) can emit at one of two resonance wavelengths located at the both sides of the stop-band, see a solid blue curve in Fig. 3(c), and the parameter tuning implied jumping between these two resonances can be expected in simulations. The gain dispersion, in this case, can be exploited for the suppression of one of the resonances [21, 12].

Lorentzian approximation of the material gain function. There are several methods for introduction of the frequency-selective gain dispersion into the time-domain TW model. Many of these approaches use an additional digital filtering of the numerically calculated optical field time series [30, 31, 32, 33, 34]. In some cases, these digital filters are equivalent to the numerical schemes obtained by discretization of some additional integrodifferential operators or differential equations. For the purpose of the analysis of the model equations, it is preferable to introduce the frequency band limiting elements directly into the model equations. For example, the TW model extensions admitting Lorentzian approximation of the material gain dispersion curves can be given by convolution integrals [34] or by an equivalent set of the linear first-order ODEs [35, 21]. Another approach to model more sophisticated gain function profiles within the TW modeling frame by including nonlinear polarization equations was used, for example, in Refs. [36, 22, 37].

In this work, we follow the strategy proposed in Refs. [21, 12]. For this reason, we approximate the gain profile in the frequency domain by a Lorentzian with the amplitude $\bar{g}$, the full width at the half maximum $\bar{\gamma} = \frac{2\pi c_0}{\lambda_0^2}\bar{\gamma}_\lambda$, and the detuning of the peak frequency $\bar{\omega} = -\frac{2\pi c_0}{\lambda_0^2}\bar{\lambda}$. Here, $\bar{\gamma}_\lambda$ and $\bar{\lambda}$ are the wavelength representations of the Lorentzian width and its peak position. In the time domain, this approximation is represented by the additional linear operator $\mathcal{D}$ in the TW

field equations, and a pair of linear differential equations for polarization functions $P^{\pm}(z,t)$:

$$\begin{array}{l} \frac{n_g}{c_0}\partial_t E^{\pm} = \mp\partial_z E^{\pm} - i\left(\beta - i\mathcal{D}\right)E^{\pm} - i\kappa E^{\mp} + F^{\pm}_{sp}, \quad z \in S_1, \\ \mathcal{D}E^{\pm} = \frac{\bar{g}}{2}\left(E^{\pm} - P^{\pm}\right), \quad \partial_t P^{\pm} = \frac{\bar{\gamma}}{2}\left(E^{\pm} - P^{\pm}\right) + i\bar{\omega}P^{\pm}, \quad z \in S_1. \end{array} \tag{14}$$

The introduction of operator $\mathcal{D}$ also implies the following modification of the stimulated recombination function $\mathcal{S}$ entering the carrier rate equations (4):

$$\mathcal{S}(N, E^{\pm}) = \frac{c_0}{n_g}\Re\langle(E, [g(N) - 2\mathcal{D}]E)\rangle_1. \tag{15}$$

To understand the impact of the operator $\mathcal{D}$, we consider the laser response function $F_l(b_1,\omega)$ again according to the modified TW model (14). When repeating the procedure described at the beginning of this section, the factor $\mathcal{B}$ entering Eq. (11) takes the form

$$\mathcal{B}(\omega) = \beta + \frac{\omega n_g}{c_0} + \chi(\omega), \text{ where } \chi(\omega) = \frac{\bar{g}}{2}\frac{(\omega-\bar{\omega})}{\bar{\gamma}/2 + i(\omega-\bar{\omega})}, \ -i\mathcal{D}\widehat{E}(z,\omega) = \chi(\omega)\widehat{E}(z,\omega). \tag{16}$$

Thus, an introduction of the linear dispersion operator $\mathcal{D}$ implies modifications of both, gain and refractive index change functions. The total gain (twice the imaginary part of $\beta - (\delta_0 - i\alpha/2) + \chi(\omega)$) and the refractive index change function (real part of the same factor), in this case, are given by the expressions

$$G(N,\omega) = g(N) - \frac{\bar{g}(\omega-\bar{\omega})^2}{(\bar{\gamma}/2)^2 + (\omega-\bar{\omega})^2}, \quad \tilde{N}(N,\omega) = \tilde{n}(N) + \frac{\bar{g}}{4}\frac{\bar{\gamma}(\omega-\bar{\omega})}{(\bar{\gamma}/2)^2 + (\omega-\bar{\omega})^2}. \tag{17}$$

Dashed curves in Figs. 3(b) and (c) illustrate the impact of the introduced gain dispersion. Whereas these corrections in the case of DFB lasers [panel (c)] are small, for the FP lasers they provide an efficient wavelength selection mechanism.

It is noteworthy that vanishing factor κ in the field equations (14), (2) implies the following simple expression of the monochromatic field *transmission* through the laser section:

$$\widehat{E}^{+}(b_1,\omega) = e^{-i\mathcal{B}(\omega)|S_1|}\widehat{E}^{+}(a_1,\omega), \quad \widehat{E}^{-}(a_1,\omega) = e^{-i\mathcal{B}(\omega)|S_1|}\widehat{E}^{-}(b_1,\omega),$$

where $\mathcal{B}(\omega)$ is defined in (16). Thus, the TW equations (14), (2) with vanishing functions $g(N)$ and $\tilde{n}(N)$, large Lorentzian amplitude $\bar{g}$, and small Lorentzian width $\bar{\gamma}$ can be effectively used for modeling of the optical filters, i.e., for extracting field frequency components located close to the relative frequency $\bar{\omega}$.

Further modifications of the model for material gain dispersion. The gain peak $g(N)$ and the simple Lorentzian dependence on the optical frequency determined by three fixed parameters $\bar{g}$, $\bar{\gamma}$ and $\bar{\omega}$ define the material gain profile $G(N,\omega)$ in Eq. 17. To improve fitting of the gain profiles obtained by calculations of microscopic models for various values of N, one can replace these three factors by appropriately selected carrier dependent functions $\bar{g}(N)$, $\bar{\gamma}(N)$, and $\bar{\omega}(N)$. In the cases, when the gain spectrum has two and more peaks or the asymmetry of the single peak is important, one can also introduce an additional set or several sets of polarization functions $P^{j\pm}(z,t)$. The gain dispersion operator $\mathcal{D}$ and corresponding total gain and

refractive index functions, in this case, read as

$$\mathcal{D}^{(s)}E^{\pm} = \sum_{j=1}^{s} \frac{\bar{g}_j}{2}\left(E^{\pm} - P^{j\pm}\right), \qquad \partial_t P^{j\pm} = \frac{\bar{\gamma}_j}{2}\left(E^{\pm} - P^{j\pm}\right) + i\bar{\omega}_j P^{j\pm}, \quad z \in S_1,$$

$$G(N,\omega) = g(N) + 2\Im\chi^{(s)}(\omega), \;\; \tilde{N}(N,\omega) = \tilde{n}(N) + \Re\chi^{(s)}(\omega), \;\; \chi^{(s)}(\omega) = \sum_{j=1}^{s} \frac{\bar{g}_j}{2} \frac{(\omega-\bar{\omega}_j)}{\bar{\gamma}_j/2 + i(\omega-\bar{\omega}_j)},$$

where s is the number of polarization function sets. Since the maximal value of $2\Im\chi(\omega)$ is, in general, smaller than zero, one should also correct the function $g(N)$.

Concluding the discussion of this section, we note that a proper numerical resolution of the gain and refractive index functions (17) for the broad frequency band when simulating the time-domain TW mode requires a careful selection of the numerical algorithm and temporal discretization steps. The size of the frequency band that can be represented by calculated discrete time series is inversely proportional to the time step, whereas the precision of the numerical simulations when approaching borders of this band are rapidly degrading. Thus, a suitable time discretization step should ensure that all important frequency regions (Bragg resonances, surrounding of a gain peak frequency, a frequency of optically injected beams, if present) are within the central part of the allowed frequency band.

4 Thermal detuning

Let us switch now to the consideration of the thermal effects. An increase of the bias current implies changes of the device temperature and, consequently, changes in the refractive index and the lasing wavelength. To model these thermal tuning effects in our device, we supplement the propagation factor β from (2) with an additional thermal detuning term $\tilde{n}_T$ [38, 14]:

$$\beta = \delta_0 + \tilde{n}(N) + \tilde{n}_T(I) + \frac{i(g(N)-\alpha)}{2}, \qquad \tilde{n}_T = \frac{2\pi n_g}{\lambda_0^2}\nu_1^1 I. \tag{18}$$

The linear thermal detuning function $\tilde{n}_T(I)$ determines the impact of the injection current I to the refractive index change. The factor ν_1^1 in solitary lasers determines an approximate red shift of the lasing wavelength due to increased bias current:

$$\nu_1^1 \approx \frac{\Delta_\lambda}{\Delta_I},$$

Here, Δ_I is the bias current tuning interval, whereas Δ_λ is the (continuous) lasing wavelength change during this current tuning.

Figs. 4(a) and (c) show the simulated wavelength change with the increased bias current in the solitary FP and DFB lasers, respectively. Here, besides of the dominant optical modes shown in white, one can see other slightly excited optical modes which are (almost) equidistant in the FP case (a) or indicate the DFB laser resonance located on the other side of the stopband. The estimated wavelength shift $\frac{\Delta_\lambda}{\Delta_I} \approx 3.14$ nm/A obtained for the FP laser and 3.09 nm/A for the DFB laser slightly differs from the factor $\nu_1^1 = 3.2$ nm/A used in our simulations. We attribute this slight discrepancy to the additional contribution of the full refractive index change function $\tilde{N}(N,\omega)$ defined in Eq. (17). Namely, the dependence of the carrier density N and

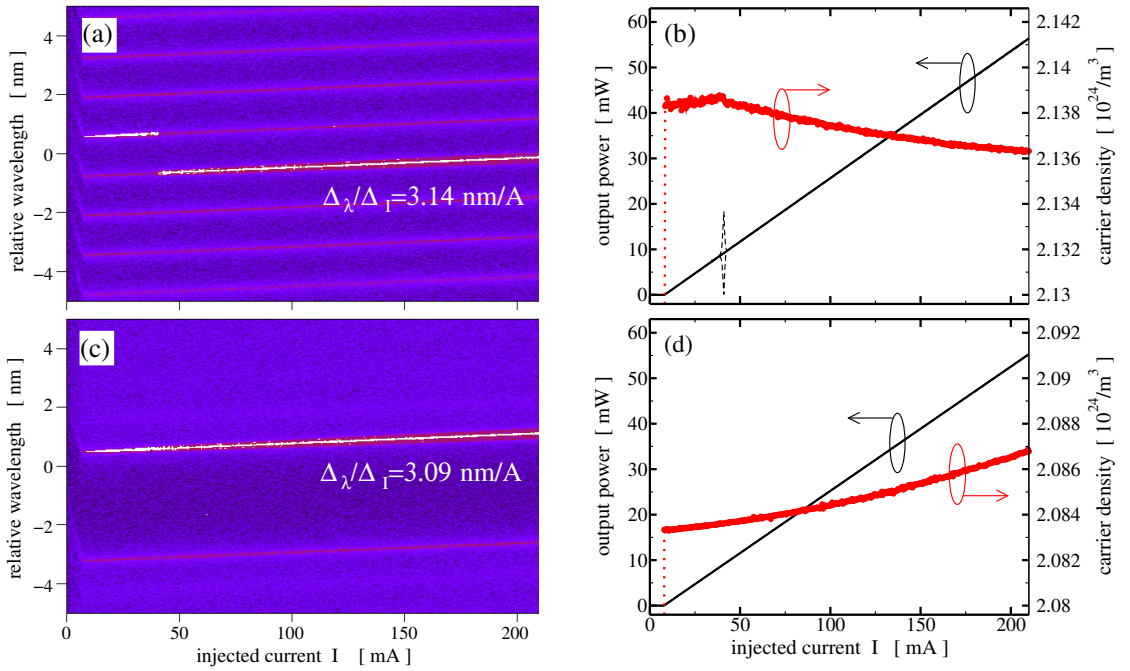

Figure 4: Mapping of the optical spectra (a), (c) and mean emitted power and carrier density (b), (d) as functions of the increased injected current I in solitary FP (a), (b) and DFB (c), (d) lasers. $\sigma = 2 \cdot 10^{-13}\,\mathrm{m}^2$, $A = 2 \cdot 10^8/\mathrm{s}$, $B = 1 \cdot 10^{-16}\,\mathrm{m}^3/\mathrm{s}$, $C = 1.3 \cdot 10^{-41}\,\mathrm{m}^6/\mathrm{s}$, $\nu_1^1 = 3.2 \cdot 10^{-9}\,\mathrm{m/A}$, whereas other parameters are the same as in Figs. 3(b) and (c) in the case of non-vanishing gain dispersion. White lines and light shading in (a) and (c) represent main and side peaks of the calculated optical spectra. Solid black and red curves in (b) and (d) show time-averaged emission intensity and carrier density, respectively. Dashed black: minima and maxima of the emission intensity.

the relative lasing wavelength λ on the bias current I (see red curves in Figs. 4 (b), (d) and wavelength shifts in Figs. 4 (a), (c), respectively) implies non-vanishing changes of the function $\tilde{N}(N,\omega) = \tilde{N}(N, -\lambda c_0/\lambda_0^2)$ which counteracts the thermal detuning term $\tilde{n}_T(I)$ and slightly reduces the red shift of the lasing wavelength.

It is noteworthy that an introduction of the thermal detuning term $\tilde{n}_T$ in our still simple TW model of the solitary laser implies, in general, only a continuous tuning of the lasing frequency. Once achieving threshold, the carrier density changes only slightly (red curves in panels (b) and (d) of Fig. 4), whereas emitted field intensity increases linearly without a visible saturation (black curves in the same panels), which is still not taken into account in our model. This linear growth of the lasing wavelength can be correctly understood when analyzing TW field equations (1) with the propagation factor β defined by (18) and neglected gain dispersion. Due to the transfer matrix formalism (10), (11) and the expression of $\mathcal{B}$ in (11), the extension of β by the non-vanishing real term $\tilde{n}_T$ is equivalent to the change of the relative frequency ω by $-\tilde{n}_T c_0/n_g$, or, alternatively, the change of λ by $\frac{-\lambda_0^2}{2\pi c_0}\frac{-\tilde{n}_T c_0}{n_g} = \nu_1^1 I$.

The unique more complicated feature in Fig. 4 is the transition between two states in the FP laser at $I \approx 40\,\mathrm{mA}$, see panels (a) and (b). Fig. 4 (a) shows that in the vicinity of the transition,

these two states are determined by two optical modes belonging to the opposite slopes of the wavelength-dependent gain profile with the peak wavelength at $\bar{\lambda} = 0$. Due to the red shift, all optical modes located on the falling [increasing] slope of this gain profile undergo an increase [decrease] of the detuning from the gain peak wavelength and, consequently, a slight rise [fall] in the mode threshold N, see the red curves in panel (b) for $I < 40$ mA [$I > 40$ mA]. A similar increase of the dominant falling-gain-slope mode threshold can also be seen in Fig. 4 (d). At the position of the state transition, the wavelengths of two involved modes are symmetric with respect to the gain peak wavelength and, what is more important, their thresholds become equal. Due to a further tuning of the bias current, the previously suppressed mode at the increasing gain profile slope becomes the minimal threshold mode, is amplified and, finally, turns to be the dominant one. See Refs. [26, 14, 15] for more details on similar and more complex mode transitions.

Modeling of crosstalk heating effects in multisection devices. In MSLs devices, one can also use a more advanced model for thermal detuning function $\tilde{n}_T$ which takes into account local and nonlocal cross-talk heating effects [38]:

$$\tilde{n}_T|_{z\in S_k} = \tilde{n}_{T,k} = \frac{2\pi n_{g,k}}{\lambda_0^2} \sum_{r=1}^{m} \nu_k^r I_r. \tag{19}$$

Here, m is a number of sections in the considered MSL. The coefficients ν_k^r of the linear thermal detuning function $\tilde{n}_T(I)$ determine the impact of the injection currents I_r attributed to the sections S_r on the refractive index change within each laser section S_k.

The effect of the thermal detuning in MSLs is much more complicated than that one of the solitary laser. Besides of the red shift of the lasing wavelength, the MSLs can also exhibit periodically or almost periodically reappearing transitions between different states. The change of mean carrier density in various sections during each such period between state changes can be significant and can not be explained by simple gain saturation or detuning from the gain peak effects. In some cases, a measured variation of the lasing wavelength with an increase or decrease of the injection current in different laser sections, together with the analysis of the field equations provide good estimates of thermal detuning coefficients including cross-talk effects [38, 14, 15].

Another well-known effect occurring with the heating of the semiconductor laser is the red shift of the gain peak wavelength [39]. If required, these changes can be accounted by the relation [38]

$$\bar{\lambda}|_{z\in S_k} = \bar{\lambda}_k = \bar{\lambda}_k^0 + \sum_{r=1}^{m} \bar{\nu}_k^r I_r, \tag{20}$$

which is quite similar to the thermal detuning relation (19). Here, $\bar{\lambda}_k^0$ denotes an injection-independent part of the gain peak wavelength in the section S_k, and $\bar{\nu}_k^r$ are linear thermal gain peak detuning coefficients. When applying these expressions, one should be aware that a proper numerical time-domain resolution of a significant (tens or even hundreds of nanometers) gain peak shift requires very small time and, consequently, space discretization steps.

5 Spatially inhomogeneous carrier density

Another important extension of the basic TW model takes into account sectionally inhomogeneous distributions of carrier density N. Namely, in this case, the sectionally averaged carrier density function $N(t)$ is replaced by the spatially distributed function $N(z,t)$, $z \in S_1$. This model extension can be especially important in the situations admitting localization of the high-intensity fields within the laser cavity, which takes place, for example, during propagation of ultrashort optical pulses in mode-locked lasers, or DBR lasers with a high coupling factor κ. Due to stimulated recombination, the high-intensity fields at these localized regions can significantly deplete the carrier distribution causing a spatial hole burning (SHB) of the carriers [40, 12].

To achieve a quantitative description of spatial hole burning, we replace simple carrier rate equation (4) by the following equation for spatially distributed carrier density:

$$\begin{aligned} &\partial_t N(z,t) = \mathcal{J}(I,N) - \mathcal{R}(N) - \mathcal{S}(N,E^{\pm}), \quad z \in S_1, \\ &\mathcal{J}(I,N(z,t)) = \tfrac{1}{q\sigma|S_1|}\left[I + \tfrac{U_F'}{r_S}\left(\langle N\rangle_1 - N(z,t)\right)\right]. \end{aligned} \tag{21}$$

Here, $\mathcal{J}$ is the inhomogeneous injection current density [41, 42, 12], N and $\langle N\rangle_1$ are spatially distributed and sectionally averaged carrier densities, U_F' and r_s denote the derivative of the Fermi level separation with respect to N and the series resistivity, whereas $\mathcal{S}$ is the spatially distributed stimulated recombination function,

$$\mathcal{S}(N,E^{\pm}) = \tfrac{c_0}{n_g}\Re\left(E,[g(N) - 2\mathcal{D}]E\right). \tag{22}$$

In the case of the limit $r_s \to 0$, the spatially distributed carrier density, $N(z,t)$, at each position z converges to the sectional average, $N(t) = \langle N\rangle_1$. Since the sectional averaging of Eqs. (21), (22) yields the equations (4), (15), the TW models with and without spatial distribution of carriers in this limit case are equivalent.

Fig. 5 shows some effects occurring due to the SHB of carriers in solitary DFB lasers. The impact of the SHB depends on the injection level. Just above the lasing threshold, the field intensity is small, and the carrier density remains nearly homogeneous, having only a small dip in the center of the laser. With raising injection, this dip increases, but, due to a simultaneous increase of the carrier density at the facets, the mean density remains nearly constant: see only slightly increasing $\langle N\rangle_1$ for $I \leq 90$ mA in panel (b) of the same figure. At these small-to-moderate bias current levels, the carrier density remains symmetric with respect to the laser centrum (dashed curve in panel (c)), and emission at the both facets is the same (see coinciding red and blue curves in panel (a) for $I \leq 90$ mA and panel (f) at $I = 70$ mA). The inhomogeneous carrier density (dashed curve in Fig. 4(d)) causes a corresponding longitudinal variation of the index of refraction. The Bragg resonance of the grating thus has not the identical spectral position along the section but varies over a considerable portion of the stop band [12]. As a consequence, the symmetry of the stop band is lost, and the laser preferably operates on the short wavelength side of its stop band [see Figs. 4(f)]. The preference of the short-wavelength mode is also shown by the laser response functions $F_l(b_1,\omega)$ and $F_r(a_1,\omega)$ [see Figs. 4(e)] calculated for spatially distributed carrier density profile (dashed curve in Fig. 4(d)) at $I = 70$ mA according to the formulas (10), (11), (12), and the algorithm explained in Section 3.

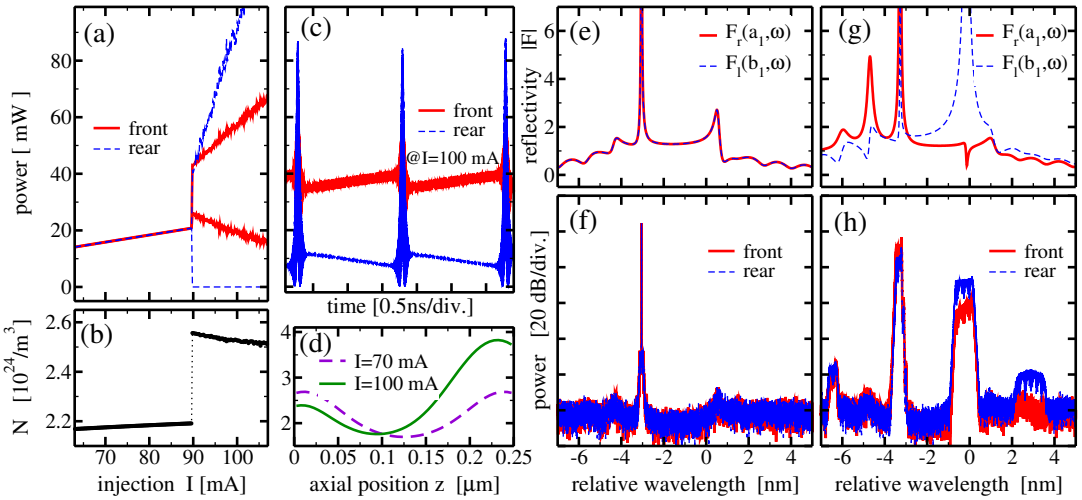

Figure 5: Spatial hole burning in solitary DFB laser. Minimal and maximal output power at both facets (a) and sectionally averaged carrier density $\langle N \rangle_1$ (b) as functions of increased bias current. (c): Time trace of the emitted field intensity at both facets for fixed $I = 100\,\text{mA}$. (d): Time-averaged carrier densities for $I = 70\,\text{mA}$ and $I = 100\,\text{mA}$. DFB reflectivity spectra (e), (g) and calculated optical spectra (f), (h) for $I = 70\,\text{mA}$ (e), (f) and $I = 100\,\text{mA}$ (g), (h). Red and blue curves in panels (a), (c), (e)-(h) represent optical fields at the front (J_1) and rear (J_2) facets of the laser. $U'_F = 10^{-25}\,\text{Vm}^3$, $r_S = 5\,\Omega$, whereas other parameters are the same as in Figs. 4 (c) and (d) except $\nu_1^1 = 0$.

At $I \approx 90\,\text{mA}$, the symmetric solution loses its stability in symmetry breaking pitchfork bifurcation [43]. According to Refs. [43, 12], the supercritical pitchfork bifurcation of the stable symmetric steady state in DFB lasers generates a pair of new stable steady states with asymmetric density profiles (each one the mirror of the other). In our case, the pitchfork bifurcation seems to be of the subcritical type. Instead of finding two asymmetric stable steady states, we immediately jump to the pulsating state with different emission at both laser facets and larger mean carrier density (see panels (a) and (b) for $I > 90\,\text{mA}$, respectively). The spatial distribution of the carrier density, in this case, is strongly asymmetric, see a solid curve in panel (d). This asymmetry together with non-commuting intermediate transfer matrices M_s from (12) implies differences in DFB laser response functions estimated at the front (F_r) and the rear (F_l) sides of the laser, see Fig. 5 (g). The optical spectra of the emission at the both sides of the laser [Fig. 5 (h)] also reveal these differences. Like the response functions of the panel (g), the left (red curves) and the right (blue curves) facet emissions have more pronounced contributions at the shorter and longer wavelength sides of the stop band, respectively.

6 Nonlinear gain saturation

Until now, our phenomenological models for peak gain and refractive index change (3) were taking into account their dependence on the sectionally averaged or local carrier density N. It is known, however, that the high-intensity optical fields saturate the gain function. To account for

such saturation, one can introduce the following modifications of the gain and refractive index functions which should be used for the definition of the propagation factor β in (2) or (18) and stimulated recombination function $\mathcal{S}$ in (6), (15), or (22):

$$g(N,E^{\pm})=g(N)\rho_G(E^{\pm}),\qquad \tilde{n}(N,E^{\pm})=\tilde{n}(N)\rho_I(E^{\pm}),$$
$$\text{where}\qquad \rho_j=\begin{cases}(1+\varepsilon_j|E|^2)^{-1}, & \text{if } N=N(z,t)\\ (1+\varepsilon_j\|E\|^2)^{-1}, & \text{if } N=N(t)\end{cases},\quad j=G,I.$$

Two different parameters, ε_G and ε_I, separately define the nonlinear gain and refractive index dependence on the local or spatially averaged optical field intensity. A typical assumption $\varepsilon_G=\varepsilon_I$ relates the gain and refractive index functions by the linewidth enhancement factor α_H. Another reasonable assumption $\varepsilon_I=0$, $\varepsilon_G>0$ [44] used for modeling of high power amplifiers considers the nonlinear compression of the gain function alone.

The importance of the nonlinear gain compression is best visible in high-power lasers and optical amplifiers showing several Watt emission intensity [44]. Some impact of the gain compression in small-to-moderate (≤ 100 mW) intensity regimes can also be observed when operating in the vicinity of various bifurcations, where a small change of parameters implies qualitative changes of the operating states. We should note, however, that the gain compression, in this case, implies only small shifts of the bifurcation positions, but has no significant impact on the qualitative description of laser dynamics in a large parameter domain. An analysis of simple TW model equations (1), (4) can explain the little influence of the gain compression in these regimes. A non-vanishing gain compression depletes the gain function $g(N)$ what implies a growth of the carrier density needed to reach threshold gain condition g_{th}. In solitary lasers, this growth is given by factor $g_{\text{th}}\varepsilon_G|E|^2/(g'\Gamma)$, which for typical gain compression coefficients and small-to-moderate field intensities is not exceeding a few percents of threshold carrier density. Consequently, a similar (up to a few percent) decay of the emission intensity can be observed.

A somehow different situation occurs in semiconductor ring lasers [19, 22, 45, 23], where a proper introduction of nonlinear gain compression is crucial when deciding the type of operation states. In this case, one should distinguish the gain compression implied by co- and counter-propagating fields:

$$g^{\pm}(N,E^{\pm})=g(N)\rho_G^{\pm}(E^{\pm}),\qquad \tilde{n}^{\pm}(N,E^{\pm})=\tilde{n}(N)\rho_I^{\pm}(E^{\pm}),$$
$$\text{where}\qquad \rho_j^{\pm}=\begin{cases}(1+\varepsilon_{js}|E^{\pm}|^2+\varepsilon_{jc}|E^{\mp}|^2)^{-1}, & \text{if } N=N(z,t)\\ (1+\varepsilon_{js}\langle|E^{\pm}|^2\rangle+\varepsilon_{jc}\langle|E^{\mp}|^2\rangle)^{-1}, & \text{if } N=N(t)\end{cases},\quad j\in\{G,I\},\tag{23}$$

whereas parameters ε_{js} and ε_{jc}, $j=G,I$, determine self- and cross- saturation of the gain and refractive index functions. In the ring lasers, usually is assumed that $\varepsilon_{Gc}>\varepsilon_{Gs}$ and $\varepsilon_{Ic}>\varepsilon_{Is}$. A detailed analysis based on the Maxwell-Bloch equations showed that the cross-saturation factor for two resonant modes in the ring cavity is twice larger than the self-saturation one [46].

The generalized functions $g^{\pm}$ and $\tilde{n}^{\pm}$ enter the definition of the propagation factor $\beta=\beta^{\pm}$ and

the stimulated recombination function $\mathcal{S}$:

$$\beta^{\pm} = \delta_0 + \tilde{n}^{\pm}(N, E^{\pm}) + \tilde{n}_T(I) + \tfrac{i(g^{\pm}(N,E^{\pm})-\alpha)}{2},$$
$$\mathcal{S}(N, E^{\pm}) = \begin{cases} \frac{c_0}{n_g}\Re\sum_{\nu=\pm} E^{\nu *}[g^{\nu}(N, E^{\pm}) - 2\mathcal{D}]E^{\nu}, & \text{if } N = N(z,t) \\ \frac{c_0}{n_g}\Re\sum_{\nu=\pm} \langle E^{\nu *}[g^{\nu}(N, E^{\pm}) - 2\mathcal{D}]E^{\nu}\rangle_1, & \text{if } N = N(t) \end{cases} . \quad (24)$$

It is noteworthy that differences in parameters ε_{js} and ε_{jc}, $j = G, I$, imply differences in the propagation factors β^+ and β^- determining the evolution of the fields E^+ and E^-, respectively. These differences are crucial when determining type and stability of operating states in the ring laser, see Refs. [19, 45, 23] for more details.

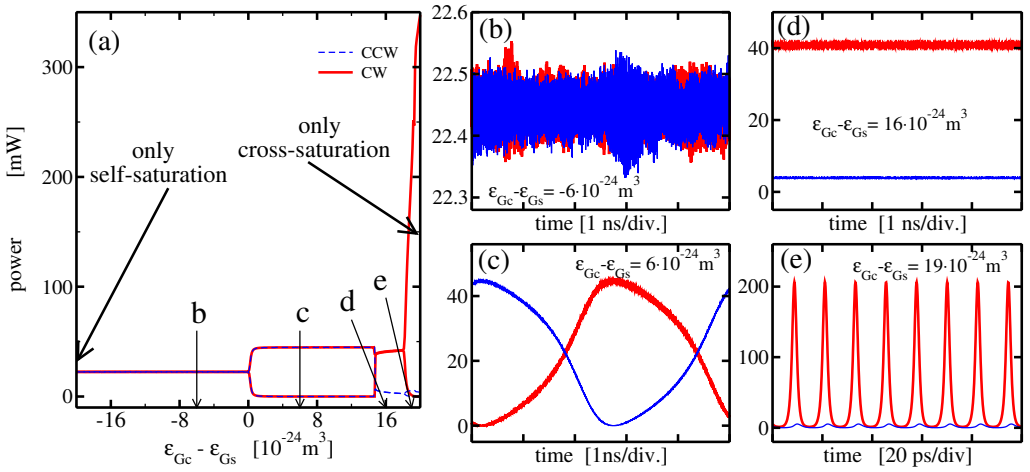

Figure 6: Dynamic regimes for different contributions of the cross- and self- gain saturations. (a): Maximal and minimal intensities of the optical fields at J_1 for changing values of $\varepsilon_{Gc} - \varepsilon_{Gs}$ but fixed $\varepsilon_{Gs} + \varepsilon_{Gc} = 20 \cdot 10^{-24}\,\mathrm{m}^3$. (b)-(e): Typical representatives of the observed regimes. Red and blue: clockwise and counter-clockwise propagating fields. Parameters are similar to those of Figs. 4(a) and (b), only $|S_1| = 1000\,\mu\mathrm{m}$, $\alpha_H = -2$, $\alpha = 2\,\mathrm{cm}^{-1}$, $\nu_1^1 = \varepsilon_{Is} = \varepsilon_{Ic} = 0$, $I = 100\,\mathrm{mA}$. U_F' and r_S are the same as in Fig. 5, whereas the field transmission and localized backscattering parameters at J_1 are $t_1 = \sqrt{0.7}$ and $r_1 = 0.007$, respectively.

To illustrate how an asymmetry of the self- and cross- gain saturation implies different operation states in the ring laser [see Fig. 2 (b)], we have simulated the TW model equations (14), (21), (8), (5), (22), (23), (3) for vanishing ε_{Is} and ε_{Ic}, fixed non-vanishing sum $\varepsilon_{Gc} + \varepsilon_{Gs} = C > 0$ and tuned difference $\varepsilon_{Gc} - \varepsilon_{Gs}$. Fig. 6 shows the results of these simulations. Solid red and dashed blue curves in all panels of this figure represent clock-wise (CW) and counter-clockwise (CCW) propagating field functions $E^-(b_1, t)$ and $E^+(a_1, t)$ at the point scattering source J_1, respectively [see Fig. 2 (b)]. Panel (a) of this figure gives an overview of all obtained states when tuning $\varepsilon_{Gc} - \varepsilon_{Gs}$ from $-C$ (full self-saturation with vanishing ε_{Gc}) up to $+C$ (full cross-saturation with vanishing ε_{Gs}). Panels (b)-(e) of the same figure represent four different observed dynamic regimes. The first three regimes occurring with a consequent increase of the cross-gain saturation are the bidirectional stable stationary state (b), the alternate oscillations (c), and the unidirectional bistable state (d). These three regimes can be observed experimentally and recovered

theoretically using a simple two-mode ODE model [19]. An analysis of the TW model performed in Ref. [23] has explained the relation between the asymmetry of the gain compression factors, ε_{Gc} and ε_{Gs}, and stability of the bidirectional steady state (regime b) or unidirectional bistable states (regime d). It was also shown, how the difference $\beta^+ - \beta^-$ and localized backscattering r_1 determine the frequency of alternating oscillations (regime c).

The last simulated regime (e) was observed for the dominant cross-gain saturation. Like usual mode-locking pulsations, this regime is characterized by large short pulses occurring with the round-trip period. However, in contrast to the mode-locking observed in multisection ring lasers [47], this state is unidirectional and does not require any fast saturable absorption. Similar mode-locked pulsations in a single-section ring laser were found and discussed theoretically in Ref. [45].

7 Further modifications of the TW model

There exist a vast number of further possible modifications of the TW model for MSLs. Each of these modifications, however, requires a few new not very well known parameters and, therefore, should be used with great care. On the other hand, some of these modifications being crucial when analyzing a particular group of MSLs can be irrelevant for simulations and analysis of different type MSLs. Below we present several modifications of the TW model used for investigation of specific types of MSLs.

Multiple carrier rate equations in quantum-dot lasers. Once modeling QD lasers, one should take into account carrier exchange processes between a carrier reservoir (CR) and discrete levels in quantum dots.

One of the simplest ways to account for all these transitions within the TW modeling frame is provided by the rate equations for the normalized carrier density $N^{cr}(z,t)$ (scaled by the factor Θ_{N}) within the CR, and occupation probabilities $N^{gs}(z,t)$, $N^{es}(z,t)$ of the ground state (GS) and the first excited state (ES) of QDs, respectively [48, 10, 49].

To keep the structure of the TW field equations (14) unchanged, we neglect the inhomogeneous spectral broadening effect due to QD non-uniformity and consider a simple single-Lorentzian gain spectrum profile, which limits the material gain bandwidth. Besides, we assume that the laser operates at the GS transition only. In this case, the propagation factor β depends on the ground state occupation probability $N^{gs}(z,t)$ only. The expression of $\beta(N^{gs})$ is equivalent to that one given by Eqs. (2) and (3) with spatially distributed occupation probability $N^{gs}(z) \in [0,1]$ and factor $1/2$ instead of the carrier density $N(z,t)$ and transparency carrier density N_{tr}, respectively.

To describe carrier exchange processes between the CR, GS, and ES of the QDs in the active

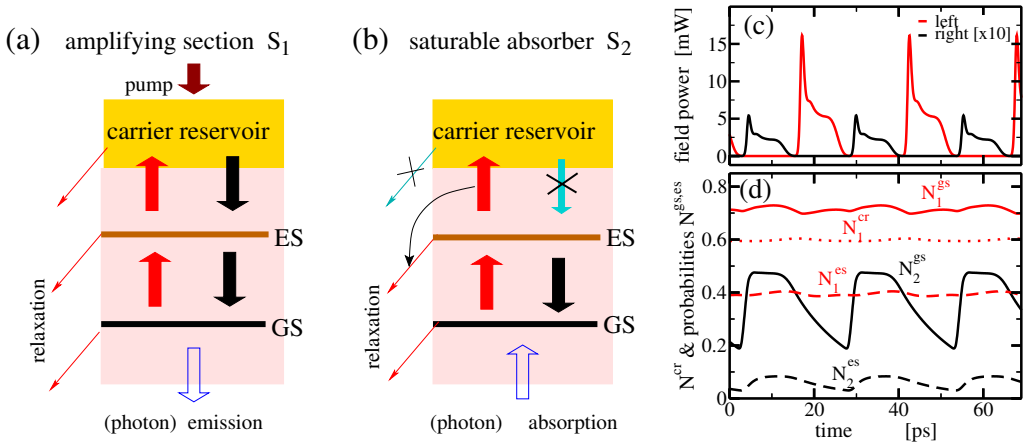

Figure 7: Schematic representation of carrier transitions in the gain section (a) and the saturable absorption section (b) of the QD MSL. Crossed arrows in panel (b) indicate the transitions which are neglected in the model equations. A sequence of the emitted mode-locking pulses with an enhanced trailing edge plateaux at both sides of the laser (c) and the sectionally averaged carrier functions $N^{gs,es,cr}$ in both laser sections (d). All parameters and a detail description of the MSL device can be found in Refs. [10, 49].

section [see Fig. 7(a)], we use the following set of rate equations:

$$\begin{aligned}
\tfrac{d}{dt}N^{gs}(z,t) &= -\tfrac{N^{gs}}{\tau_{gs}} + 2\left(\tfrac{N^{es}(1-N^{gs})}{\tau_{es\to gs}} - \tfrac{N^{gs}(1-N^{es})}{2\tau_{gs\to es}}\right) - \tfrac{1}{\theta_E}\mathcal{S}(N^{gs},E^{\pm}),\\
\tfrac{d}{dt}N^{es}(z,t) &= -\tfrac{N^{es}}{\tau_{es}} - \left(\tfrac{N^{es}(1-N^{gs})}{\tau_{es\to gs}} - \tfrac{N^{gs}(1-N^{es})}{2\tau_{gs\to es}}\right) + \left(\tfrac{N^{cr}(1-N^{es})}{4\tau_{cr\to es}} - \tfrac{N^{es}}{\tau_{es\to cr}}\right), \qquad (25)\\
\tfrac{d}{dt}N^{cr}(z,t) &= \tfrac{I}{q|S_1|\theta_I} - \tfrac{N^{cr}}{\tau_{cr}} - 4\left(\tfrac{N^{cr}(1-N^{es})}{4\tau_{cr\to es}} - \tfrac{N^{es}}{\tau_{es\to cr}}\right).
\end{aligned}$$

Here, $\mathcal{S}(N^{gs},E^{\pm})$ is defined by (22), whereas τ_a^{-1} and $\tau_{a\to b}^{-1}$, $a,b\in\{gs,es,cr\}$, denote spontaneous relaxation and transition rates between GS, ES, and CR, respectively. Factors $(1-N^{gs})$ and $(1-N^{es})$ represent the Pauli blocking, factors 2 and 4 account for the spin degeneracy in the QD energy levels. Note, that here we neglect direct transitions between CR and GS. θ_I and $\theta_E=\frac{2hc_0\theta_I}{\lambda_0}$ are scaling factors relating the injection current I, the field intensity $|E|^2$, the CR scaling factor θ_N, the differential gain g', and the QD density in the active zone.

In the saturable absorption sections [see Fig. 7(b)], there is no pumping, $I=0$, so that the transitions from CR to ES can be neglected, $\tau_{cr\to es}\to\infty$, and the CR equation in (25) can be ignored. The carrier transition from ES to CR can be added to similar spontaneous recombination term: $\bar\tau_{es}^{-1}=\tau_{es}^{-1}+\tau_{es\to cr}^{-1}$. Following Ref. [48], one can model the carrier transitions in the negatively driven saturable absorber by assuming an exponential decay of $\bar\tau_{es}$ with growing negative voltage U, whereas all other relaxation rates remain unchanged.

Figs. 7(c) and (d) present an example of simulated mode-locked quantum dot laser containing an amplifying and a saturable absorber sections S_1 and S_2. Panel (c) of this figure gives an evidence of strongly asymmetric pulses with a broad trailing edge plateau. Our theoretical analysis has shown that such pulses arise mainly due to non-instant carrier transitions between the CR, ES, and GS of the QD laser shown in panel (d) of the same figure. The presence of these tran-

sitions exert a smoothening effect on all spatial/temporal carrier and field intensity distributions and, in turn, imply a broadening of the trailing edge of the pulse. We have also found that an increase of the intra-dot transition rates leads to a reduction of the filtering effect and, hence, to a growth of the pulse peak intensity and narrowing of the pulse and its trailing edge. More details on our analysis as well as experimental demonstration of such asymmetric pulses can be found in Refs. [10, 49].

Further modifications of the TW model can be used for more precise simulations of QD lasers. For example, one can improve the model of carrier transitions (25) by separate consideration of electrons and hole densities [50]. To allow a simultaneous radiation on the spectrally well separated ground and excited states, one can introduce another pair of TW equations for optical fields [51]. An inhomogeneous spectral broadening and an accompanying description of the radiation at GS and ES can also be modeled by an introduction of multiple sets of carrier rate and polarization equations representing carrier transitions within the QDs of different size and their impact on the laser emission at different wavelengths [52].

Nonlinear gain and refractive index functions. In the discussion above, the gain and the refractive index dependence on the carrier density N was modeled by linear functions related to each other by the linewidth enhancement factor α_H. This modeling approach is reasonable for small and slow variation of carrier density N, but can fail once N exhibits some significant changes, see, e.g., Fig. 5(d), where a variation of the spatially distributed $N(z,t)$ was of the order of the mean value of the carrier density. In such situations, one should better use nonlinear peak gain functions, $g(N)$, which can better represent measured or pre-calculated gain spectra profiles. For this reason, the following logarithmic gain peak function dependence on the carrier density is frequently used:

$$g(N) = \Gamma g' N_{\text{tr}} \ln\left(\frac{\max\{N,N^*\}}{N_{\text{tr}}}\right), \qquad \tilde{n}(N) = \frac{\alpha_H g(N)}{2}. \tag{26}$$

Here, N^* indicates a cutoff carrier density value which prevents the convergence $g(N) \to -\infty$ with carriers $N \to 0$. These expressions for the gain and index change functions replace the relations (3) in the TW models discussed above.

Another issue is related to the linewidth enhancement factor α_H. Initially, this factor was used to relate gain and refractive index functions at a fixed value of N. Such approach implies a rather simple model for propagation factor, β, and can be quite useful when performing an advanced analysis of model equations. In reality, however, the ratio between the gain and refractive index is not a constant, but a function depending on carrier density, temperature and several other factors not discussed in this paper. Thus, an experimental estimation of this factor in the semiconductor laser operating at different conditions or using different methods can lead to rather different values of α_H. For this reason, it can be preferable to use separately defined nonlinear peak gain and index change functions $g(N)$ and $\tilde{n}(N)$. These functions depend on the properties of the semiconductor material and the design of the device, and, therefore, should be adjusted individually for each considered laser.

A satisfactory description of these functions for a broad class of semiconductor lasers is given

by the logarithmic, and the square root like expressions [38],

$$g(N) = \Gamma g' N_{\text{tr}} \ln\left(\frac{\max\{N,N^*\}}{N_{\text{tr}}}\right), \qquad \tilde{n}(N) = \tilde{n} + \alpha_H \, \Gamma g' \sqrt{N \cdot N_{\text{tr}}}. \tag{27}$$

Here, $\tilde{n}$ represents the offset of the refractive index change function, $\Gamma g' = \partial_N g(N_{\text{tr}})$, and $\alpha_H = 2\partial_N \tilde{n}(N_{\text{tr}}) / \partial_N g(N_{\text{tr}})$ is the linewidth enhancement factor evaluated at the transparency carrier density N_{tr}.

We should admit, however, that linear formulas (3) with slightly corrected factors g', α_H, N_{tr}, and a proper selection of δ_0 can be used for approximation of nonlinear functions (27) not only in the vicinity of N_{tr} but also over a larger range of densities N including the threshold density N_{th}. In many cases, the simplifications of the gain and refractive index functions still imply qualitatively the same results when performing simulations of MSLs with varying parameters [53].

8 Multisection lasers and coupled laser systems

A vast variety of MSLs and coupled laser systems can be represented as a set of differently interconnected laser sections, each characterized by its material and geometry parameters. To distinguish these parameters or functions attributed to different laser sections we shall use the lower indices. For example, α_k, $g_k(N)$, and a_k denote the field losses, the gain function and the left edge coordinate of the section S_k. Note also, that for unique identification of longitudinal coordinate z within all laser sections, different sections of our device are represented by non-overlapping intervals $[a_k, b_k]$.

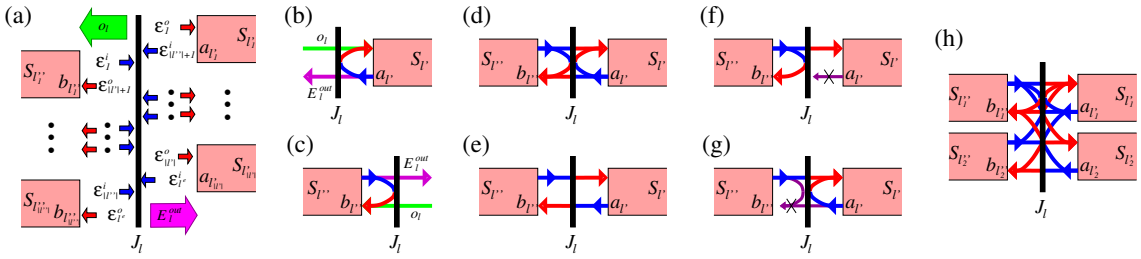

Figure 8: Schematic representation of different interfaces between the sections at the junction J_l. (a): general configuration. (b) and (c): field reflection and optical injection at laser facets. (d) and (e): reflecting (transmission and reflection) and trivial (transmission only) interface of two section edges. (f) and (g): directionally absorbing interfaces of two section edges for modeling of a master-slave laser system. (h): transmitting/reflecting interface of four section edges for modeling ring lasers with an outcoupling waveguide. Black segments and pink frames represent junction J_l and all section edges connected to this junction, respectively. Blue and red arrows in all diagrams represent all components of the vector fields $\mathcal{E}_l^i$ and $\mathcal{E}_l^o$, respectively. Optical injections o_l and emitted fields E_l^{out} are shown by green and violet arrows. Crossed arrows in panels (f) and (g) represent a full absorption of the corresponding fields.

According to our laser device construction, for any edge of all sections S_k, we can attribute a unique junction J_l. On the other hand, each junction has, at least, one section joining it from

one or another side, see, e.g., Fig. 1, where MSLs are represented as sets of laser *sections* mutually interconnected through different *junctions*. To explain the relations between section edges, corresponding junctions and applied optical injections, we use the following notations in the formulas below. By l we denote the index of the junction J_l, as well as optical fields and the section edges attributed to this junction. l' (l'') is the vector of length $|l'|$ ($|l''|$) containing indices of the sections connected to J_l by their left (right) edge $a_{l'_j}$ ($b_{l''_j}$), see Fig. 8(a). $l^e = |l'| + |l''| \geq 1$ is a total number of such section edges connected to J_l. By $o_l(t)$ and $E_l^{\text{out}}(t)$ we denote the applied optical injection and the recorded emission at the same junction, see thick green and violet arrows in Fig. 8(a). When the injection or emission at J_l is absent, the corresponding function is simply set to zero.

General field scattering conditions at the arbitrary junction J_l are defined by the $l^e \times l^e$ dimensional complex field scattering matrix $\mathcal{T}_l$, $l^e \times 1$ dimensional injection distribution matrix $\mathcal{T}_l^i$, and $1 \times l^e + 1$ outcoupling matrix $\mathcal{T}_l^o$:

$$\begin{aligned}
&\mathcal{E}_l^o = \mathcal{T}_l \mathcal{E}_l^i + \mathcal{T}_l^i o_l, \quad E_l^{\text{out}} = \mathcal{T}_l^o \begin{pmatrix} \mathcal{E}_l^i \\ o_l \end{pmatrix}, \qquad \text{where} \\
&\mathcal{E}_l^o = \left(E^+_{l'_1}(a_{l'_1}, t), \ldots, E^+_{l'_{|l'|}}(a_{l'_{|l'|}}, t), E^-_{l''_1}(b_{l''_1}, t), \ldots, E^-_{l''_{|l''|}}(b_{l''_{|l''|}}, t) \right)^T, \\
&\mathcal{E}_l^i = \left(E^+_{l''_1}(b_{l''_1}, t), \ldots, E^+_{l''_{|l''|}}(b_{l''_{|l''|}}, t), E^-_{l'_1}(a_{l'_1}, t), \ldots, E^-_{l'_{|l'|}}(a_{l'_{|l'|}}, t) \right)^T.
\end{aligned} \tag{28}$$

The vector functions $\mathcal{E}^i$ and $\mathcal{E}^o$ (see blue and red arrows in Fig. 8(a)) denote the internal optical fields which are incident into the junction from all adjacent sections and are scattered from the junction back into these sections, respectively.

In most cases, the interfaces between the sections are much simpler. For example, the scattering matrices at the facets of the solitary laser [panels (b) and (c) of Fig. 8 as well as junctions J_1 and J_2 in Fig. 2(a)] are determined by the boundary conditions (7), i.e.,

$$\begin{cases} \mathcal{T}_l = -r_l^*, \ \mathcal{T}_l^i = 1, \ \mathcal{T}_l^o = (t_l, 0), & \text{single "left" edge } a_{l'}, \ |l'| = 1, \ |l''| = 0 \\ \mathcal{T}_l = r_l, \ \mathcal{T}_l^i = 1, \ \mathcal{T}_l^o = (t_l, 0), & \text{single "right" edge } b_{l''}, \ |l''| = 1, \ |l'| = 0 \end{cases}, \tag{29}$$

were r_l and t_l are field reflection and transmission coefficients,

$$|r_l| \leq 1, \qquad t_l \leq \sqrt{1 - |r_l|^2}. \tag{30}$$

Another frequently used case in MSLs is the interface of two adjacent sections [panels (d) to (g) of Fig. 8]. At such interfaces, we have no optical injections and field emission, so that we can set $\mathcal{T}_l^i = (0, 0)^T$ and $\mathcal{T}_l^o = (0, 0, 0)$. The scattering of the field at J_l, in this case, is entirely defined by the 2×2 dimensional matrix

$$\mathcal{T}_l = \begin{pmatrix} t_l & -r_l^* \\ r_l & t_l \end{pmatrix}, \tag{31}$$

where t_l and r_l satisfy the conditions (30) [see Fig. 8(d) and, e.g, J_3 in Fig. 1(a)]. Here, the non-vanishing reflections r_l can appear, e.g., due to different heterostructure of the adjacent

sections. In the simplest case of $r_l = 0$ and $t_l = 1$, $\mathcal{T}_l$ is an identity matrix, and the interface admits a full transmission of the optical fields (see Fig. 8(e) and J_2 in Fig. 1(a)).

When modeling the master-slave laser system [S_1 and S_2 in Fig. 1(d)], only one-directional field propagation should be allowed in the air gap between two lasers (section S_3 in the same figure). This effect can be achieved by modification of otherwise standard scattering matrices $\mathcal{T}_l$ (31) at one of the gap section edges. One can model a full absorption of the backward incident beam at the interface of the master laser and the gap section [see Fig. 8(f) and J_2 of Fig. 1(d)], or prohibit the field backscattering into the air gap at the interface of the slave laser and the gap section [Fig. 8(g) and J_3 of Fig. 1(d)]. Formally, both these situations can be defined by the scattering matrices

$$\mathcal{T}_j = \begin{pmatrix} t_j & 0 \\ r_j & 0 \end{pmatrix} \text{ (master-gap interface)}, \qquad \mathcal{T}_j = \begin{pmatrix} t_j & -r_j^* \\ 0 & 0 \end{pmatrix} \text{ (gap-slave interface)}.$$

More complicated situations occur at the junctions connecting more than two section edges of the MSL. For example, Fig. 8(h) and J_1 of Fig. 1(e) represent an interface connecting two "left" and two "right" section edges. This situation is used for modeling of a localized coupling of the ring laser [section S_1 in Fig. 1(e)] and the outcoupling waveguide (S_2 and S_3 in the same figure).

Similarly to the previously discussed case, the optical injection- and field emission- relevant matrices can be defined by $\mathcal{T}_l^i = (0,0,0,0)^T$ and $\mathcal{T}_l^o = (0,0,0,0,0)$. By assuming a non-vanishing field reflection r_l at the ring laser part of this junction [section edges $b_{l_1''}$, $a_{l_1'}$ in Fig. 8(h) or b_1, a_1 in Fig. 1(e)], we model a *localized* linear backscattering of the fields [37, 23]. The 4×4 dimensional scattering matrix $\mathcal{T}_l$, in this case, can be defined as

$$\mathcal{T}_l = \begin{pmatrix} t_l & i\tilde{t}_l & -r_l^* & 0 \\ i\tilde{t}_l & t_l & 0 & 0 \\ r_l & 0 & t_l & i\tilde{t}_l \\ 0 & 0 & i\tilde{t}_l & t_l \end{pmatrix}, \qquad t_l^2 + \tilde{t}_l^2 + |r_l|^2 \leq 1. \tag{32}$$

Here, t_l is a real field amplitude transmission factor within the same (ring or outcoupling) waveguide and $i\tilde{t}_l$ is an imaginary coefficient representing part of the field amplitude which is outcoupled from the ring or transmitted into the ring from the external waveguide. It is noteworthy, that a proper estimation of the transmission - reflection - outcoupling matrix $\mathcal{T}_l$ in the ring laser case requires some appropriate measurements or an advanced modeling. Such modeling should take into account the curvature of the ring cavity, the length of the coupling regions, the field diffraction, and the overlapping of the lateral modes in the coupling region [54]. Moreover, the coefficients of the scattering matrix are, in general, frequency-dependent. In our TW modeling approach, we use constant coefficients describing field scattering at the central reference frequency.

9 Simulations of a complex MSL device

The concept of differently interconnected *sections* and *junctions* allows modeling rather complicated MSLs. One of such nontrivial configurations is a semiconductor ring laser with four separate branches of the filtered optical feedback, see Fig. 9(a). The multi-channel feedback scheme

of this laser admits a fast switching between steady states determined by the resonances of the ring laser and the wavelengths of the activated filtering channels [55].

Colored frames in Fig. 9(a) represent device sections of different types. Namely, we distinguish here the amplifying sections $S_{A.}$, where the field and carrier dynamics is governed by the full TW model (14), (21), (23), (5), (24), (26), and two kinds of passive sections, $S_{P.}$ and $S_{F.}$, where gain and refractive index functions are set to zero, allowing to ignore the carrier rate equations at all. The notations of all sections in the section indexes are made according to the cardinal directions “n”, “e”, “s”, and “w”.

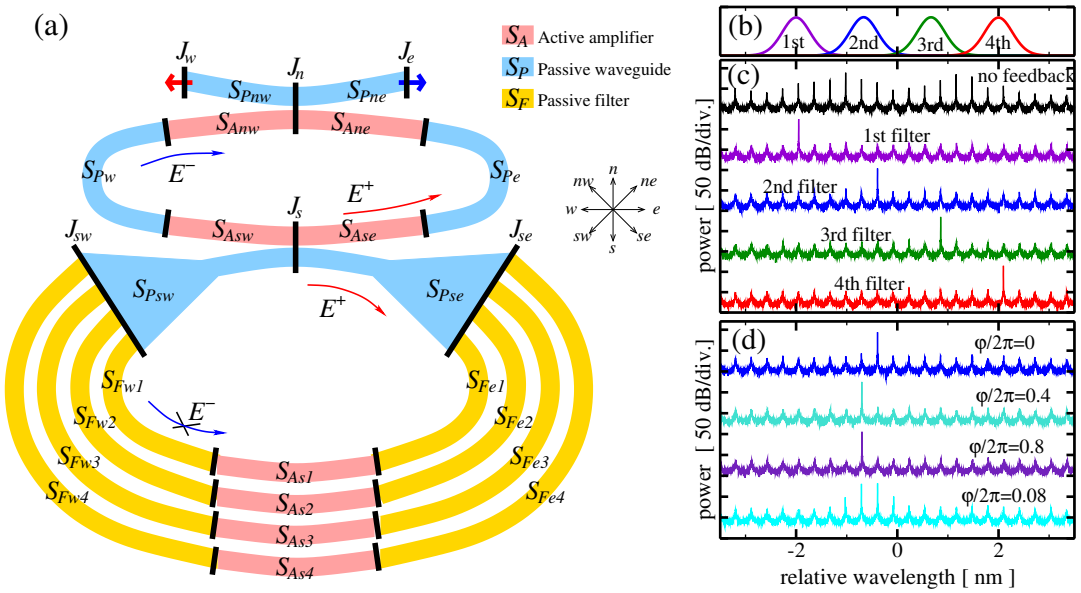

Figure 9: (a): Scheme of the semiconductor ring laser with four branches of filtered and amplified unidirectional optical feedback. Black segments and colored frames indicate junctions and different sections of the MSL. Red and blue arrows show propagation directions and the emission of the fields E^+ and E^-, respectively. (b): Transmission spectra of four filtering branches. Maximal transmission at $I_{Asj} = 10\,mA$, $j = 1, \ldots, 4$ is approximately 1.4. (c): Stabilization of the multi-mode behavior of the ring laser (black) by the single-branch filtered feedback (colored). (d): Dependence of the lasing wavelength on the feedback phase once the second filtering branch is activated.

Almost all parameters of the TW model in all sections of our MSL are the same as in Fig. 6. A few exceptions are parameters $\alpha_H = -4$ and $\bar{\gamma}_\lambda = 100\,\text{nm}$. In the passive waveguiding sections, $S_{P.}$ (light blue), we assume $|S_{Pe}| = |S_{Pw}| = 330\,\mu\text{m}$, $|S_{Pne}| = |S_{Pnw}| = 50\,\mu\text{m}$, $|S_{Pse}| = |S_{Psw}| = 2500\,\mu\text{m}$, and neglect the gain dispersion, $\bar{g} = 0$. In the passive filtering sections, $S_{F.}$ (yellow), we assume $|S_{F.}| = 530\,\mu\text{m}$ and significantly modify the profile of Lorentzian gain dispersion by setting $\bar{g} = 5 \cdot 10^4\,\text{m}^{-1}$ and $\bar{\gamma}_\lambda = 4\,\text{nm}$. The relative peak wavelengths of four filtering branches (sections S_{Fwj} and S_{Fej}, $j = 1, \ldots, 4$) are $\bar{\lambda} = -2\,\text{nm}$, $-0.67\,\text{nm}$, $0.67\,\text{nm}$, and $2\,\text{nm}$, respectively. Finally, in the amplifying sections (pink) within the primary ring laser, S_{Ajk}, $j = n, s$ and $k = e, w$, we use $|S_{A.}| = 380\,\mu\text{m}$, $\varepsilon_{Gs} = 6 \cdot 10^{-24}\,\text{m}^3$, $\varepsilon_{Gc} = 2\varepsilon_{Gs}$, and the bias currents $I = 26\,\text{mA}$, which is 1.5 times higher than the lasing threshold in the

laser without feedback. In the amplifying sections belonging to the four filtering branches, S_{Asj}, $j = 1, \ldots, 4$, we assume $|S_{A\cdot}| = 190\,\mu$m and $\varepsilon_{Gc} = \varepsilon_{Gs} = 9 \cdot 10^{-24}\,\mathrm{m}^3$. Once the bias current in these sections is zero, $I = 0$ mA, the feedback branches are efficiently absorbing the optical fields. To activate one of the feedback branches, we set the corresponding injection $I = 10$ mA.

The field transmission and reflection conditions at J_n and J_s are given by (32) with $r = 0$, $t = \sqrt{0.8}$, and $\tilde{t} = \sqrt{0.2}$. At J_{se} and J_{sw}, we neglect all possible reflectivity, admit full field transmission from filtering branches to the passive waveguide sections S_{Psw} or S_{Pse}, equally distribute the intensity of the optical field E^+ propagating from S_{Pse} to the filtering branches, and fully absorb E^- at J_{sw}:

$$E^-(b_{Pse}, t) = \textstyle\sum_{j=1}^{4} E^-(a_{Fej}, t), \qquad E^+(a_{Fej}, t) = \sqrt{\tfrac{1}{4}}\, E^+(b_{Pse}, t), \quad j = 1, \ldots, 4;$$
$$E^+(a_{Psw}, t) = \textstyle\sum_{j=1}^{4} E^+(b_{Fwj}, t), \qquad E^-(b_{Fwj}, t) = 0, \quad j = 1, \ldots, 4.$$

At J_w and J_e, the fields E^+ and E^- are emitted from our MSL. Here, the field reflection-transmission conditions are given by (29) with the reflectivity factors $r_w = r_e = 0.1$. All other junctions of this MSL are trivial, i.e., the optical fields cross the interfaces according to the relations (31) with $r_l = 0$ and $t_l = 1$.

A series of simulations represented in the remaining panels of Fig. (9) are in good agreement with the experimental results reported in Ref. [55]. First of all, panel (b) shows the transmission spectra (modulus of the wavelength dependent complex transmission function) of the optical fields E^+ propagating through each of four optical feedback branches activated by the injected current into the corresponding amplifying section. For 10 mA injections used in these simulations, the peak amplitude transmission is around 1.6.

Panels (c) and (d) of Fig. (9) show simulated optical spectra of the emitted field at the "west" facet J_w of the MSL for different operation conditions. The upper black curve in panel (c) represents the optical spectrum in the case of deactivated feedback branches. Multiple significant spectral peaks with the mode separation corresponding to the field round-trip time in the ring laser indicate a multi-mode lasing of the laser. An optical field E^+ propagating along the filtering branches, however, is not entirely absorbed. For higher ring laser injections we observed the steady states determined by a single ring resonance mode. In these cases, the amplifier within corresponding filtering branch was optically pumped, and the related peak amplitude transmission was around 0.2. The competition between nominally equivalent unpumped filtering branches, however, does not allow predicting the lasing wavelength of such a steady state.

Four lower spectra in Fig. (9)(c) represent switching between different optical modes by activation of the corresponding filter and deactivation of the remaining ones. A close inspection of these spectra shows, that whereas the first and the fourth filters select the resonance modes which are closest to the filter peak position, the third, and, especially, the second filter prefers modes admitting smaller optical feedback. We have found, that this mode selection is related to the phase of the optical field within the filtering branch. Fig. (9)(d) demonstrates, how tuning of the feedback phase within the second filtering branch (realized by variation of the detuning factor $\delta_{0,Fw2}$) implies changes between the resonant modes located within the filtering band.

In conclusion, we have simulated the MSL consisting of 22 sections interconnected at 18 junc-

tions. Our theoretical findings were in a good qualitative agreement with experimental observations of similar ring laser device reported in Ref. [55].

10 Beyond numerical simulations of the TW model

In the previous sections, we have introduced different modifications of 1+1 dimensional TW model suited for simulations of various MSL devices and coupled laser systems. In the remaining part of this work, we introduce the concept of instantaneous optical modes and present several applications of these modes for an advanced analysis of MSLs. In all these cases, we consider MSLs without optical injection and neglect a contribution of Langevin noise term $F_{sp}^{\pm}$, which is of minor importance in the lasers operating well above threshold.

Instantaneous optical modes. The concept of optical modes plays a significant role in understanding laser dynamics in general. They represent the natural oscillations of the electromagnetic field and determine the optical frequency and the lifetime of the photons contained in the given laser cavity. The *instantaneous* optical modes correspond to a fixed *instant* distribution of the propagation factor β [26].

In general, comparing to a variation of the optical fields, the changes of the carrier density N are slow. The change of N is mainly determined by the carrier relaxation time τ_N (5) which, typically, is measured in nanoseconds (or tens of picoseconds when considering saturable absorbers). On the other hand, picosecond or sub-picosecond time windows are sufficient for significant changes of the photon densities. Since the gain compression for small and moderate field intensities is also small, the propagation factor β experiences only minor modifications in the picosecond range. For this reason, below we analyze the field equations for the frozen distribution of the propagation factor $\beta(z, t_0)$ at the time instant t_0.

The instantaneous optical modes of MSLs are pairs $(\Omega(\beta), \Theta(\beta, z))$ of complex frequencies Ω and vector-functions $\Theta = (\Theta_E^+, \Theta_E^-, \Theta_P^+, \Theta_P^-)^T$, where imaginary and real parts of $\Omega(\beta)$ are mainly defining the angular frequency and the damping of the mode, whereas $\Theta(\beta, z)$ determines the spatial distribution of the mode.

Complex frequencies Ω and vector-functions $\Theta(\beta, z)$ solve the linear system of algebro-differential equations

$$\begin{cases} \frac{d}{dz}\Theta_E^+ = -i\mathcal{B}(\Omega)\Theta_E^+ - i\kappa\Theta_E^- \\ \frac{d}{dz}\Theta_E^- = i\mathcal{B}(\Omega)\Theta_E^- + i\kappa\Theta_E^+ \\ \Theta_P^{\pm}(\beta, z) = \frac{\bar{\gamma}/2}{\bar{\gamma}/2+i(\Omega-\bar{\omega})}\Theta_E^{\pm}(\beta, z) \end{cases}, \quad z \in S_k|_{k=1}^n, \qquad \theta_l^o(\beta) = \mathcal{T}_l\theta_l^i(\beta)\Big|_{l=1}^m, \tag{33}$$

obtained by assuming a stationary propagation factor, $\partial_t\beta = 0$, and substituting the expressions

$$E^{\pm}(z, t) = \Theta_E^{\pm}(\beta; z)e^{i\Omega(\beta)}, \qquad P^{\pm}(z, t) = \Theta_P^{\pm}(\beta; z)e^{i\Omega(\beta)}$$

into the field equations (14) within each of n sections S_k, and boundary conditions (28) at each of m junctions J_l. Similarly to the vector functions $\mathcal{E}_l^o$ and $\mathcal{E}_l^i$ in (28), complex vectors $\theta_l^i(\beta)$ and

$\theta_l^o(\beta)$ in (33) represent functions $\Theta_E^{\pm}(\beta, z)$ at the section edges $z = a_{l'_j}$ or $z = b_{l''_j}$ connected by the junction J_l. The function $\mathcal{B}(\Omega)$ entering (33) is defined in (16).

Each pair of linear ODEs in (33) can be solved by the transfer matrix[2] (11) with the coefficients nonlinearly depending on still unknown complex frequency Ω. These matrices define $2n$ homogeneous linear equations relating $4n$ components of the complex vector $\mathcal{S} = (s_1, \ldots, s_{4n})^T$ representing field functions $\Theta_E^{\pm}(\beta, z)$ at both edges of all sections S_k. Another $2n$ homogeneous linear equations relating the same complex numbers are given by the field scattering matrices $\mathcal{T}_l$ at all junctions J_l. In such a manner we build a linear $4n$ dimensional algebraic system

$$\mathcal{M}(\beta, \kappa; \Omega)\mathcal{S} = 0,$$

determined by a sparse $4n \times 4n$ dimensional matrix $\mathcal{M}$. Nontrivial solutions $\mathcal{S}$ (i.e., nontrivial functions Θ of the problem (33)) are available only for those Ω which are the complex roots of the complex characteristic equation

$$\det \mathcal{M}(\beta, \kappa; \Omega) = 0. \tag{34}$$

The finite number of these roots can be found using Newton iterations and the homotopy method, see Ref. [26] for more details.

It is noteworthy that linear configurations of MSLs admit rather simple expressions of characteristic equation (34) involving the response functions $F_l(z, \Omega)$ and $F_r(z, \Omega)$ defined at some longitudinal position z of the MSL:

$$\det \mathcal{M}(\beta, \kappa; \Omega) = 0 \qquad \Leftrightarrow \qquad F_l^{-1}(z, \Omega) = F_r(z, \Omega). \tag{35}$$

For example, for solitary lasers considered in Figs. 3(b) and (c), $F_l(b_1, \Omega)$ is defined in (13), whereas $F_r(b_1, \Omega) = r_2$. In the general case, functions F_l and F_r are defined by a consequent superposition of the sectional transfer matrices $M(\beta, \kappa, \Omega)$ and the left-to-right or right-to-left junction-transfer matrices

$$\mathcal{T}_{j,22}^{-1} \begin{pmatrix} \det \mathcal{T}_j & \mathcal{T}_{j,12} \\ -\mathcal{T}_{j,21} & 1 \end{pmatrix} \qquad \text{or} \qquad \mathcal{T}_{j,11}^{-1} \begin{pmatrix} 1 & -\mathcal{T}_{j,12} \\ \mathcal{T}_{j,21} & \det \mathcal{T}_j \end{pmatrix},$$

see Refs. [26, 28, 23] for more details.

The calculated optical field function $\Psi(z, t) = (E^+, E^-, P^+, P^-)^T$ can be represented as a superposition of the suitably normalized vector functions $\Theta(\beta, z)$ which are slowly changing with a variation of the propagation factor $\beta(z, t)$:

$$\Psi(z, t) = \sum_{j=1}^{\infty} f_j(t)\Psi_j(\beta(z, t), z). \tag{36}$$

Here, $f_j(t)$ is the complex amplitude of the mode, which can denote the mode contribution to the field emission at the laser facet a_k once normalization of mode functions assumes

[2] In the case of non-vanishing $\Delta_\beta = \frac{\beta^+ - \beta^-}{2}$, the transfer matrix in each section S_k should be constructed for $\bar{\beta} = \frac{\beta^+ + \beta^-}{2}$ and later multiplied by the factor $e^{-i\langle\Delta_\beta\rangle_k |S_k|}$ [23]

$\Theta_E^-(\beta, a_k) = 1$. According to our notations, index $_1$ denotes the most significant mode having a largest (instant) amplitude $|f|$ or a lowest damping $\Im\Omega$. An increasing index means a decreasing importance of the mode. This numbering does allow us to achieve good approximations of the field function $\Psi(z,t)$ already by low-dimensional truncated mode expansions (36).

Calculation of optical modes and expansion of the field function into the modal components can give a broad understanding of different operating regimes in MSLs and explain parameter change induced transitions between these states observed in simulations and experiments. We have applied our mode analysis for interpretation of experimental observations in different MSLs. Namely, we have explained a stable operation of ring lasers at alternating oscillation or bi- and uni- directional steady state regimes [23]; almost periodically reappearing state transitions and estimation of thermal tuning parameters in master-oscillator power-amplifier device [56, 38], DBR laser [14], or external cavity diode laser [15]; and strongly asymmetric pulse shapes in quantum-dot mode-locked laser [49]. More theoretical examples of our mode analysis can be found in [26].

Steady states Any stationary (rotational wave) state of the MSL is determined by an optical mode with a *real* mode frequency $\hat{\omega}$:

$$(\Psi(z,t), N(z,t)) = \left(\hat{f}\,\Theta(\hat{\beta}, z)e^{i\hat{\omega}t}, \hat{N}(z)\right), \text{ where } \Omega(\hat{\beta}) = \hat{\omega} \in \mathbb{R},$$

and $\hat{\beta}(z)$ is constant in time spatially distributed propagation factor. Let us consider the TW model with sectionally averaged carrier density and neglected nonlinear gain compression, (14), (18), (4), (5), (15), (28). In this case, all steady states are fully defined by a set of $n_a + 2$ real numbers $\left(\hat{\omega}, |\hat{f}|^2, \hat{N}_1, \ldots, \hat{N}_{n_a}\right)$, which are a mode frequency, a mode intensity, and sectionally averaged carrier densities within all n_a "active" sections having non-vanishing functions g and $\tilde{n}$. The rotational invariance of the TW model implies freedom in selection of the phase of the complex mode amplitude $\hat{f}$. The set of these real numbers is a root of a nonlinear algebraic system of one complex characteristic equation and n_a real steady-state carrier rate equations:

$$\begin{aligned} &\det \mathcal{M}\left(\beta(\hat{N}), \kappa; \hat{\omega}\right) = 0, \\ &\tfrac{I_r}{q\sigma_r|S_r|} - \mathcal{R}(\hat{N}_r) - |\hat{f}|^2 \tfrac{c_0}{n_g} G(\hat{N}_r, \hat{\omega}) \langle(\Theta_E, \Theta_E)\rangle_r = 0, \quad r = 1, \ldots, n_a. \end{aligned} \tag{37}$$

Here, the frequency dependent gain function G is defined in (17), whereas the sectional average $\langle(\Theta_E, \Theta_E)\rangle_r$ can be expressed as a function of $\hat{\omega}$ and $\hat{N}$ [28].

In the case of a single active section, $n_a = 1$, the steady state frequency $\hat{\omega}$ and threshold carrier density $\hat{N}_1$ can be directly found from the characteristic equation, whereas the remaining equation determines the value of $|\hat{f}|^2$. Assume, that the single active section S_1 of linear MSL is located on the left side of the device (see Fig. 1(b), for example), and the optical fields within the adjacent passive section S_2 are governed by the simple relations (9). For an illustration of this situation, we have considered a three section passive dispersive reflector laser consisting of the active DFB, passive DBR, and another passive phase tuning section in between. Due

to relation (35), we can replace the complex characteristic equation by a couple of real-valued equations,

$$F_l^{-1}(a_2,\hat{\omega}) = F_r(a_2,\hat{\omega}) = e^{-\alpha_2|S_2|}e^{i(\varphi-2\hat{\omega}\tau_2)}F_r(b_2,\hat{\omega}) \qquad \Leftrightarrow$$
$$\begin{cases} \tilde{\mathcal{M}}_\alpha(\hat{N}_1,\hat{\omega}) = e^{\alpha_2|S_2|} \\ 2\hat{\omega}\tau_2 - \tilde{\mathcal{M}}_\varphi(\hat{N}_1,\hat{\omega}) = \varphi \end{cases}, \tag{38}$$
$$\text{where} \quad \tilde{\mathcal{M}}_\alpha = \left|\tilde{\mathcal{M}}\right|, \quad \tilde{\mathcal{M}}_\varphi = \arg\tilde{\mathcal{M}}, \quad \tilde{\mathcal{M}}(\hat{N}_1,\hat{\omega}) = F_l(a_2,\hat{\omega})F_r(b_2,\hat{\omega}).$$

A couple of real-valued equations (38) suggest a simple way to the location of the steady

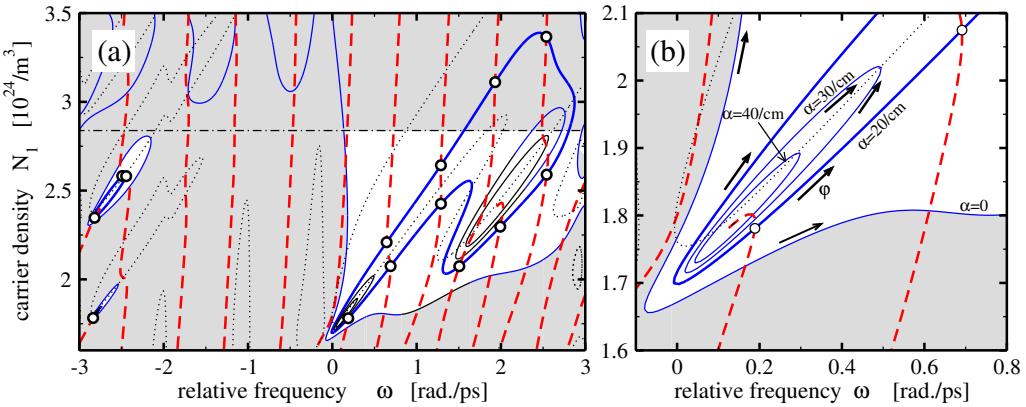

Figure 10: Stationary states (frequencies and threshold carrier densities) of a three section DFB laser. Panels (a) and (b) show a global overview and a zoomed-in region close to the minimal threshold mode with $\hat{\omega} \approx 0$. Solid black: steady states for all possible φ but only few fixed α_2. Red dashed: states for all α_2 for fixed $\varphi = 0$. Dotted: states where saddle-node bifurcation holds. Hollow bullets: steady states for $\alpha_2 = 20$/cm and $\varphi = 0$. Dash-dotted line: maximal N_1 which can be achieved for considered bias current I. Gray shading: unphysical states. Small arrows in panel (b) indicate directions of the steady state shift along the fixed loss lines for growing φ. All parameters as in Ref. [26].

states. Namely, each of these equations for fixed parameters α_2 and φ defines one or several curves in frequency ω – carrier threshold N_1 domain, see black solid and red dashed curves in Fig. 10. The intersections of these lines determine the steady state pairs $\hat{\omega}, \hat{N}_1$ (hollow bullets in the same figures). It is noteworthy, that to any point in the $\lambda - N_1$ domain one can attribute a unique triple of loss, phase and mode power parameters α_2, φ and $|\hat{f}|^2$. ω and N_1 within the gray shading regions of Fig. 10 represent the unphysical steady states corresponding to negative damping in the passive section ($\alpha_2 < 0$) and negative mode intensity ($|\hat{f}|^2 < 0$) due to insufficient pumping of the active section.

The fixed level lines of $\tilde{\mathcal{M}}_\alpha$ determined by larger losses $\alpha_2 = 30$ and 40/cm (thin solid black ellipses located inside of thick solid black curves in Fig. 10) are shrinking towards central points, which are resonances of the solitary DFB laser. Accordingly, the (odd) number of steady states on each ellipse is also reduced. The saddle-node bifurcation, which is responsible for creation or annihilation of the steady state pair, occurs at those φ and α_2, where corresponding fixed

level lines of $\tilde{\mathcal{M}}_\varphi$ and $\tilde{\mathcal{M}}_\alpha$ become tangent to each other. The last condition, formally given by

$$\mathcal{M}_{SN}(\hat{\omega}, \hat{N}_1) \stackrel{def}{=} \partial_\omega \tilde{\mathcal{M}}_\alpha \partial_{N_1} \tilde{\mathcal{M}}_\varphi - \partial_\omega \tilde{\mathcal{M}}_\varphi \partial_{N_1} \tilde{\mathcal{M}}_\alpha = 0,$$

is satisfied on the dotted lines of Fig. 10.

In general, the interpretation of the steady states for large α_2 (small feedback) is in good agreement with the analysis of the external cavity modes in the Lang-Kobayashi (LK) model of lasers with delayed feedback [18, 27]. A decrease of α_2 leads to blowing up and collision of different ellipses. This scenario involves multiple modes of the solitary DFB laser and can be no more explained by the LK model.

Mode approximation systems. For some MSL devices, the TW model (14), (2), (3), (4), (5), (15), (28) with sectionally averaged carrier densities, linear gain and index change functions and neglected gain compression terms can be reduced to a finite-dimensional system of ODEs describing an evolution of q complex mode amplitudes f and real sectionally averaged carrier densities N within n_a active sections of MSL:

$$\begin{aligned} \dot{f}_k &= i\Omega_k(N) f_k + \sum_{l=1}^{q} \left(\sum_{r=1}^{n_a} K^r_{k,l}(N) \dot{N}_r \right) f_l, \quad k = 1, \ldots, q; \\ \dot{N}_r &= \tfrac{I_r}{q|S_r|\sigma_r} - \mathcal{R}(N_r) - \Re \sum_{k,l=1}^{q} L^r_{k,l}(N) f^*_k f_l, \quad r = 1, \ldots, n_a. \end{aligned} \tag{39}$$

This mode approximation (MA) system follows from the substitution of the truncated field expansion (36) into the TW model equations and projection of the resulting field equations onto the linear subspace defined by each of q modes. The non-adjoint nature of the field evolution operator and small but non-vanishing time derivatives of propagation factor $\beta(N)$ imply the appearance of the mode coupling terms $K^r_{k,l}\dot{N}_r$. For the derivation of the MA equations and analytic expressions for carrier and mode frequency Ω dependent mode coupling functions, $K^r_{k,l}$ and $L^r_{k,l}$, see Ref. [28].

To check the precision of our MA system, we have performed simulations of the TW model and two related MA systems describing the evolution of a mode-locked laser consisting of a saturable absorber and an amplifying section (case of $n_a = 2$). Solid black curve and hollow bullets in Figs. 11(b) and (c) show typical optical spectrum and time trace of the mode-locking pulsations obtained by numerical integrations of the TW model. To determine the most relevant complex mode frequencies $\Omega(N)$ [panel (a) of the same figure] and field expansion coefficients f from (36) [bullets in panel (b)], we have used the carrier densities $N = (N_1, N_2)$, optical fields E, and polarization functions P obtained as a result of the numerical integration of the TW model. For the construction of 40MA and 50MA systems, we have used the modes indicated by full red and hatched blue bullets in Figs. 11(a) and (b). Red and blue curves in Fig. 11(c) represent the numerical integration of these MA systems. One can see, that whereas 40MA system fails to reproduce the stable periodic regime, the 50MA system provides a perfect approximation of the TW model. We note that a significant number of excited optical modes in the example considered above does not allow achieving a low dimensional approximation of the TW model. The number of active modes usually is much smaller in MSLs containing one or more DFB

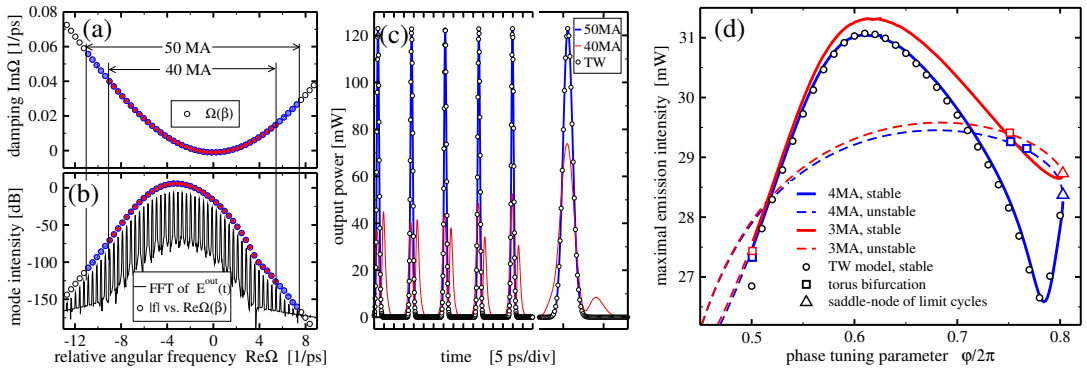

Figure 11: Calculated complex frequencies Ω (a), simulated optical spectra as a Fourier-transformed field $E^-(a_1, t)$ [black solid curve] and as a discrete set of mode intensities $|f|^2$ from Eq. (36) vs. $\Re\Omega$ [bullets] (b), and a comparison of the calculated transients of the TW model [bullets] and the reduced ODE systems determined by 40 [red] or 50 [blue] optical modes (c) in a two-section mode-locked laser. Full red and hatched blue bullets in panels (a) and (b) indicate the modes used for the construction of 40MA and 50MA systems. (d): Numerical path following of the stable periodic solution of the TW model (bullets) and periodic orbits of 3MA (red) and 4MA (blue) systems in a three-section phase-controlled mode-beating DFB laser [12, 28]. Solid and dashed curves indicate stable and unstable orbits. Hollow boxes and triangles denote torus and fold bifurcations, respectively.

sections. In this case, already three or four appropriately selected optical modes are sufficient for a good approximation of the TW model [28, 7].

An integration of the MA system (39) remains a nontrivial task, because for each actual set of carrier densities $N = (N_1, \ldots, N_r)$, one should find the corresponding mode frequencies $\Omega_k(N), k = 1 \ldots, q$ by solving the characteristic equation (34) numerically. Since the required computation time of the MA systems grows quadratically with the increasing number of modes, one can integrate the TW model faster than the above-discussed 50MA system. The usefulness of the MA approach starts to be visible when combining our model reduction technique with the numerical continuation and bifurcation analysis tools [29] suited for investigation of nearly arbitrary systems of ODEs. Fig. 11(d) presents an example of numerical bifurcation analysis of 3MA (red) and 4MA (blue) systems describing dynamics of the three-section laser consisting of two active DFB sections and a passive phase tuning section in between ($n = 3$ and $n_a = 2$ in this case). Here, solid and dashed curves represent stable and unstable branches of the periodic orbit implied by beating of two closely located resonances, supported by each DFB section. Hollow bullets in the same figure represent the continuation of the stable periodic state by direct integration of the TW model. By comparing the bullets and curves, one can see, that both MA systems were able to reproduce the stable branch of the periodic orbit, and identify torus and saddle-node bifurcations where this state has lost its stability. The deviation of the solid red curve from the bullet positions in Fig. 11(d), however, indicates the insufficiency of the 3MA system to reproduce the orbit shape. More detailed analysis of this laser including a continuation of bifurcations in two parameter domain can be found in Ref. [28].

11 Conclusions

In this work, we introduce a hierarchy of traveling wave models describing nonlinear dynamics in individual semiconductor lasers, various MSLs, and coupled laser systems. To simulate these laser devices, we use our software package LDSL-tool, which treats MSLs as a set of differently interconnected laser sections. At the end of the work, we introduce several advanced techniques allowing detailed analysis of the model equations. These methods include computation of optical modes, a study of the mode spectra, expansion of electric fields into modal components, a semi-analytic location of all steady states of the MSLs, model reduction, numerical continuation and bifurcation analysis of the reduced system. Altogether, these advanced possibilities of our software tool allow to achieve a thorough understanding of the processes observed both, in the direct integration of model equations and experiments.

References

[1] M. Fleming and A. Mooradian, "Spectral characteristics of external-cavity controlled semiconductor lasers," *IEEE J. of Quantum Electronics*, vol. 17, pp. 44–59, 1981.

[2] A. Argyris, D. Syvridis, L. Larger, V. Annovazzi-Lodi, P. Colet, I. Fischer, J. García-Ojalvo, C. Mirasso, L. Pesquera, and K. Shore, "Chaos-based communications at high bit rates using commercial fibre-optic links," *Nature*, vol. 438, pp. 343–346, 2005.

[3] A. Uchida, K. Amano, M. Inoue, K. Hirano, S. Naito, H. Someya, I. Oowada, T. Kurashige, M. Shiki, S. Yoshimori, K. Yoshimura, and P. Davis, "Fast physical random bit generation with chaotic semiconductorlasers," *Nat. Photonics*, vol. 2, no. 12, pp. 728–732, 2008.

[4] E. Murphy, "The semiconductor laser: Enabling optical communication," *Nature Photonics*, vol. 4, no. 5, p. 287, 2010.

[5] H.-J. Wünsche, O. Brox, M. Radziunas, and F. Henneberger, "Excitability of a semiconductor laser by a two-mode homoclinic bifurcation," *Phys. Rev. Lett.*, vol. 88, no. 2, p. 023901, 2002.

[6] O. Brox, S. Bauer, M. Radziunas, M. Wolfrum, J. Sieber, J. Kreissl, B. Sartorius, and H.-J. Wünsche, "High-frequency pulsations in dfb-lasers with amplified feedback," *IEEE J. of Quantum Electronics*, vol. 39, no. 11, pp. 1381–1387, 2003.

[7] M. Radziunas, A. Glitzky, U. Bandelow, M. Wolfrum, U. Troppenz, J. Kreissl, and W. Rehbein, "Improving the modulation bandwidth in semiconductor lasers by passive feedback," *IEEE J. of Selected Topics in Quantum Electronics*, vol. 13, no. 1, pp. 136–142, 2007.

[8] U. Bandelow, M. Radziunas, A. Vladimirov, B. Hüttl, and R. Kaiser, "Harmonic mode-locking in monolithic semiconductor lasers: theory, simulations and experiment," *Optical and Quantum Electronics*, vol. 38, pp. 495–512, 2006.

[9] R. Arkhipov, A. Pimenov, M. Radziunas, D. Rachinskii, A. Vladimirov, D. Arsenijevic, H. Schmeckebier, and D. Bimberg, "Hybrid mode locking in semiconductor lasers: simulations, analysis and experiments," *IEEE J. of Selected Topics in Quantum Electronics*, vol. 19, no. 4, p. 1100208, 2013.

[10] M. Radziunas, A. Vladimirov, E. Viktorov, G. Fiol, H. Schmeckebier, and D. Bimberg, "Pulse broadening in quantum-dot mode-locked semiconductor lasers: simulation, analysis and experiments," *IEEE J. of Quantum Electronics*, vol. 47, no. 7, pp. 935–943, 2011.

[11] M. Möhrle, B. Sartorius, C. Bornholdt, S. Bauer, O. Brox, A. Sigmund, R. Steingrüber, M. Radziunas, and H.-J. Wünsche, "Detuned grating multisection-RW-DFB lasers for high-speed optical signal processing," *IEEE J. of Selected Topics in Quantum Electronics*, vol. 7, no. 2, pp. 217–223, 2001.

[12] H.-J. Wünsche, M. Radziunas, S. Bauer, O. Brox, and B. Sartorius, "Simulation of phase-controlled mode-beating lasers," *IEEE J. of Selected Topics in Quantum Electronics*, vol. 9, no. 3, pp. 857–864, 2003.

[13] S. Bauer, O. Brox, J. Kreissl, B. Sartorius, M. Radziunas, J. Sieber, H.-J. Wünsche, and F. Henneberger, "Nonlinear dynamics of semiconductor lasers with active optical feedback," *Phys. Rev. E*, vol. 69, p. 016206, 2004.

[14] M. Radziunas, K.-H. Hasler, B. Sumpf, T. Q. Tien, and H. Wenzel, "Mode transitions in DBR semiconductor lasers: experiments, simulations and analysis," *J. Phys. B: At. Mol. Opt. Phys.*, vol. 44, p. 105401, 2011.

[15] M. Radziunas, V. Tronciu, E. Luvsandamdin, C. Kürbis, A. Wicht, and H. Wenzel, "Study of micro-integrated external-cavity diode lasers: simulations, analysis and experiments," *IEEE J. of Quantum Electronics*, vol. 51, no. 2, p. 2000408, 2015.

[16] O. Hess and T. Kuhn, "Spatio-temporal dynamics of semiconductor lasers: theory, modelling and analysis," *Prog. Quant. Electr.*, vol. 20, no. 2, pp. 85–179, 1996.

[17] E. Gehrig, O. Hess, and R. Walenstein, "Modeling of the performance of high power diode amplifier systems with an optothermal microscopic spatio-temporal theory," *IEEE J. of Quantum Electronics*, vol. 35, pp. 320–331, 2004.

[18] R. Lang and K. Kobayashi, "External optical feedback effects on semiconductor injection laser properties," *IEEE J. of Quantum Electronics*, vol. 16, pp. 347–355, 1980.

[19] M. Sorel, G. Giuliani, A. Scire, R. Miglierina, J. Laybourn, and S. Donati, "Operating regimes of GaAs-AlGaAs semiconductor ring lasers: experiment and model," *IEEE J. of Quantum Electronics*, vol. 39, pp. 1187–1195, 2003.

[20] A. Vladimirov and D. Turaev, "Model for passive mode-locking in semiconductor lasers," *Phys. Rev. A*, vol. 72, p. 033808, 2005.

[21] U. Bandelow, M. Radziunas, J. Sieber, and M. Wolfrum, "Impact of gain dispersion on the spatio-temporal dynamics of multisection lasers," *IEEE J. of Quantum Electronics*, vol. 37, pp. 183–188, 2001.

[22] J. Javaloyes and S. Balle, "Emission directionality of semiconductor ring lasers: a traveling-wave description," *IEEE J. of Quantum Electronics*, vol. 45, pp. 431–438, 2009.

[23] M. Radziunas, "Longitudinal modes of multisection edge-emitting and ring semiconductor lasers," *Optical and Quantum Electronics*, vol. 47, no. 6, pp. 1319–1325, 2015.

[24] U. Bandelow, R. Hünlich, and T. Koprucki, "Simulation of static and dynamic properties of edge-emitting multiple-quantum-well lasers," *IEEE J. of Selected Topics in Quantum Electronics*, vol. 9, no. 3, pp. 798–806, 2003.

[25] M. Radziunas, "LDSL-tool: a software package for simulation and analysis of longitudinal dynamics of multisection semiconductor lasers." www.wias-berlin.de/software/ldsl.

[26] M. Radziunas and H.-J. Wünsche, "Multisection lasers: longitudinal modes and their dynamics," in *Optoelectronic Devices - Advanced Simulation and Analysis* (J. Piprek, ed.), ch. 5, pp. 121–150, New York: Springer, 2005.

[27] M. Radziunas, H.-J. Wünsche, B. Krauskopf, and M. Wolfrum, "External cavity modes in Lang-Kobayashi and traveling wave models," in *SPIE Proc. Series*, vol. 6184, p. 61840X, 2006.

[28] M. Radziunas, "Numerical bifurcation analysis of the traveling wave model of multisection semiconductor lasers," *Physica D*, vol. 213, pp. 98–112, 2006.

[29] E. Doedel, A. Champneys, T. Fairgrieve, Y. Kuznetsov, B. Sandstede, and X. Wang, "AUTO97: Continuation and bifurcation software for ordinary differential equations (with HomCont)," Technical Report TW-330, Department of Computer Science, K.U.Leuven, Leuven, Belgium, 2001.

[30] S. Bischoff, J. Mørk, T. Franck, S. Brorson, M. Hofmann, K. Frojdh, and L. Prip, "Monolithic colliding pulse mode-locked semiconductor lasers," *Quantum Semiclass. Opt.*, vol. 9, no. 5, pp. 655–674, 1997.

[31] M. Kolesik and J. Moloney, "A spatial digital filter method for broad-band simulation of semiconductor lasers," *IEEE J. of Quantum Electronics*, vol. 37, no. 7, pp. 936–944, 2001.

[32] A. Lowery, "New dynamic semiconductor laser model based on the transmission-line modelling method," *IEE Proc. J*, vol. 134, no. 5, pp. 281–289, 1987.

[33] D. Jones, L. Zhang, J. Carroll, and D. Marcenac, "Dynamics of monolithic passively mode-locked semiconductor lasers," *IEEE J. of Quantum Electronics*, vol. 31, no. 6, pp. 1051–1058, 1995.

[34] E. Avrutin, J. Marsh, and E. Portnoi, "Monolitic and multi-GigaHertz mode-locked semiconductor lasers: constructions, experiments, models and applications," *IEE Proc. Optoelectron.*, vol. 147, no. 4, pp. 251–278, 2000.

[35] C. Ning, R. Indik, and J. Moloney, "Effective Bloch equations for semiconductor lasers and amplifiers," *IEEE J. of Quantum Electronics*, vol. 33, no. 9, pp. 1543–1550, 1997.

[36] M. Homar, S. Balle, and M. S. Miguel, "Mode competition in a Fabry-Perot semiconductor laser: travelling wave model with asymmetric dynamical gain," *Opt. Communications*, vol. 131, pp. 380–390, 1996.

[37] A. Pérez-Serrano, J. Javaloyes, and S. Balle, "Longitudinal mode multistability in ring and Fabry-Perot lasers: the effect of spatial hole burning," *Optics Express*, vol. 19, pp. 3284–3289, 2011.

[38] M. Spreemann, M. Lichtner, M. Radziunas, U. Bandelow, and H. Wenzel, "Measurement and simulation of distributed-feedback tapered master-oscillators power-amplifiers," *IEEE J. of Quantum Electronics*, vol. 45, no. 6, pp. 609–616, 2009.

[39] B. Grote, E. Heller, R. Scarmozzino, J. Hader, J. Moloney, and S. Koch, "Fabry-Perot lasers: temperature and many-body effects," in *Optoelectronic Devices - Advanced Simulation and Analysis* (J. Piprek, ed.), pp. 27–61, New York: Springer, 2005.

[40] H.-J. Wünsche, U. Bandelow, and H. Wenzel, "Calculation of combined lateral and longitudinal spatial hole burning in $\lambda/4$ shifted DFB lasers," *IEEE J. of Quantum Electronics*, vol. 29, no. 6, pp. 1751–1760, 1993.

[41] U. Bandelow, H. Wenzel, and H.-J. Wünsche, "Influence of inhomogeneous injection on sidemode suppression in strongly coupled DFB semiconductor lasers," *Electronics Letters*, vol. 28, pp. 1324–1325, 1992.

[42] P. Eliseev, A. Glebov, and M. Osinski, "Current self-distribution effect in diode lasers: analytic criterion and numerical study," *IEEE J. of Selected Topics in Quantum Electronics*, vol. 3, pp. 499–506, 1997.

[43] R. Schatz, "Longitudinal spatial instability in symmetric semiconductor lasers due to spatial hole burning," *IEEE J. of Quantum Electronics*, vol. 28, no. 6, pp. 1443–1449, 1992.

[44] V. Tronciu, S. Schwertfeger, M. Radziunas, A. Klehr, U. Bandelow, and H. Wenzel, "Amplifications of picosecond laser pulses in tapered semiconductor amplifiers: numerical simulations versus experiments," *Opt. Communications*, vol. 285, pp. 2897–2904, 2012.

[45] A. Pérez-Serrano, J. Javaloyes, and S. Balle, "Bichromatic emission and multimode dynamics in bidirectional ring lasers," *Physical Review A*, vol. 81, p. 043817, 2010.

[46] E. D'Angelo, E. Izaguirre, G. Mindlin, L. Gil, and J. Tredicce, "Spatiotemporal dynamics of lasers in the presence of an imperfect O(2) symmetry," *Physical Review Letters*, vol. 68, pp. 3702–3704, 1992.

[47] Y. Barbarin, E. Bente, M. Heck, Y. Oei, R. Nötzel, and M. Smit, "Characterization of a 15 GHz integrated bulk InGaAsP passively modelocked ring laser at 1.53μm," *Optics Express*, vol. 14, no. 21, pp. 9716–9727, 2006.

[48] E. Viktorov, T. Erneux, P. Mandel, T. Piwonski, G. Madden, J. Pulka, G. Huyet, and J. Houlihan, "Recovery time scales in a reversed-biased quantum dot absorber," *Appl. Phys. Lett.*, vol. 94, p. 263502, 2009.

[49] M. Radziunas, A. Vladimirov, E. Viktorov, G. Fiol, H. Schmeckebier, and D. Bimberg, "Strong pulse asymmetry in quantum-dot mode-locked semiconductor lasers," *Appl. Phys. Lett.*, vol. 98, p. 031104, 2011.

[50] K. Lüdge and E. Schöll, "Quantum-dot lasers – desynchronized nonlinear dynamics of electrons and holes," *IEEE J. of Quantum Electronics*, vol. 45, no. 11, pp. 1396–1403, 2009.

[51] A. Markus, M. Rossetti, V. Calligari, D. Chek-Al-Kar, J. Chen, A. Fiore, and R. Scollo, "Two-state switching and dynamics in quantum dot two-section lasers," *J. of Applied Physics*, vol. 100, p. 113104, 2006.

[52] M. Rossetti, P. Bardella, and I. Montrosset, "Time-domain travelling-wave model for quantum dot passively mode-locked lasers," *IEEE J. of Quantum Electronics*, vol. 47, no. 2, pp. 139–150, 2011.

[53] V. Tronciu, M. Radziunas, C. Kürbis, H. Wenzel, and A. Wicht, "Numerical and experimental investigations of micro-integrated external cavity diode lasers," *Optical and Quantum Electronics*, vol. 47, no. 6, pp. 1459–1464, 2015.

[54] T. Krauss and P. Laybourn, "Very low threshold current operation of semiconductor ring lasers," *IEE Proc. J*, vol. 139, no. 6, pp. 383–388, 1992.

[55] I. Ermakov, S. Beri, M. Ashour, J. Danckaert, B. Docter, J. Bolk, X. Leijtens, and G. Verschaffelt, "Semiconductor ring laser with on-chip filtered optical feedback for discrete wavelength tuning," *IEEE J. of Quantum Electronics*, vol. 48, no. 2, pp. 129–136, 2012.

[56] M. Radziunas, V. Tronciu, U. Bandelow, M. Lichtner, M. Spreemann, and H. Wenzel, "Mode transitions in distributed-feedback tapered master-oscillator power-amplifier: theory and experiments," *Optical and Quantum Electronics*, vol. 40, pp. 1103–1109, 2008.